**Eric
David Bosne**

Sistema de deteção Timepix e FitPix na análise de materiais em RBS/C

Timepix and FitPix detection system for RBS/C materials analysis

Eric
David Bosne

Sistema de deteção Timepix e FitPix na análise de materiais em RBS/C

Timepix and FitPix detection system for RBS/C materials analysis

"(...)
If you can meet with Triumph and Disaster
And treat those two impostors just the same;
(...)
If you can fill the unforgiving minute
With sixty seconds' worth of distance run,
Yours is the Earth and everything that's in it,
And - which is more - you'll be a Man, my son!"

— If by Joseph Rudyard Kipling (1865 − 1936)

Eric
David Bosne

Sistema de deteção Timepix e FitPix na análise de materiais em RBS/C

Timepix and FitPix detection system for RBS/C materials analysis

o júri / the jury

presidente / president

Prof. Doutor Ricardo Assis Guimarães Dias
Professor Auxiliar do Departamento de Física da Universidade de Aveiro

vogais / examiners committee

Prof. Doutor Joaquim Marques Ferreira dos Santos
Professor Catedrático do Centro de Instrumentação da Faculdade de Ciências e Tecnologia da Universidade de Coimbra

Prof. Doutor Ulrich Wahl
Investigador Principal do Centro de Ciências e Tecnologias Nucleares do Polo de Loures, Instituto Superior Técnico, Universidade de Lisboa

Palavras Chave Detetor Sensível à Posição, Timepix, Fitpix, Calibração em Energia, Espetroscopia de Retrodispersão de Rutherford, Canalização Iónica, Simulação de Monte Carlo, Cristais Únicos

Resumo

Esta tese relata a implementação de um detetor sensível à posição do tipo Timepix num laboratório de feixe de iões para uso com feixe de ^{1}H$^+$ e ^{4}He$^+$ com 2MeV colimado a 0.5mm para uso em Espetroscopia de Retrodispersão de Rutherford (RBS/C).

É dada uma descrição completa da metodologia usada para calibração em energia, análise de dados de RBS e sua simulação com o método de Monte Carlo através do programa FLUX.

A calibração em energia foi realizada por impulsos internos e a resultante resolução e precisão foram verificadas em dois modos. O primeiro usando uma fonte de partículas alfa composta pelos isótopos ^{239}Pu, ^{241}Am e ^{244}Cm e o segundo usando um espectro de RBS da medida de um filme fino de Au/SiO$_2$/C.

Caracterização do sistema de medida para experiências de canalização iónica for realizada com cristais únicos de silício (Si), carboneto de silício (6H-SiC) e titanato de estrôncio (SrTiO$_3$).

A resolução em energia alcançada foi de 47.2keV para He$^+$ a uma energia de retrodisperção de 1862keV e resolução angular de 0.11° (desvio padrão).

Foram alcançadas taxas de contagens até 2kHz com uma velocidade de frame de 15 frames/s. Taxas de contagens mais elevadas são possíveis, no entanto, tem o custo de um aumento do tempo morto do detetor.

Não foi encontrado nenhum efeito notável na resolução em energia devido a dano por radiação depois de uma fluência de 7.5×10^7 partículas/cm^2.

Keywords

Abstract

This thesis reports the implementation of a Timepix position sensitive detector in a ion beam facility with a 0.5mm collimated beam of 2MeV ^{1}H$^+$ and ^{4}He$^+$ for use in Rutherford Back-scattering Spectrometry channelling (RBS/C).

A complete description is given of the methodology used for energy calibration, RBS data analysis and simulation with the FLUX Monte Carlo simulation program.

Energy calibration was performed with internal test pulses and resulting resolution and accuracy were verified in two ways. The first time using a triple alpha source with the isotopes ^{239}Pu, ^{241}Am and ^{244}Cm and secondly using a RBS spectrum of a thin film sample of Au/SiO$_2$/C.

Setup characterization for channelling measurements was performed using single crystals of Si, 6H-SiC and SrTiO$_3$.

An energy resolution of 47.2keV at 1862keV for He$^+$ and an angular resolution of 0.11° (standard deviation) was achieved.

Count rates as high as 2kHz were achieved with a frame rate of 15 frames/s. Higher count rates are possible, however, at the cost of an increase pile-up or increase in the detector dead-time.

No radiation damage effect on the energy resolution was perceivable after a fluence of 7.5×10^7 particles/cm^2.

Contents

List of Figures

List of Acronyms

AC	Alternating Current	**NRA**	Nuclear Reaction Analysis
ADC	Analog to Digital Converter	**PC**	Personal Computer
BCA	Binary Collision Approximation	**PIGE**	Particle Induced Gamma Emission
CERN	European Organization for Nuclear Research	**PIXE**	Particle Induced X-ray Emission
DAC	Digital to Analog Converter	**PSD**	Position Sensitive Detector
DC	Direct Current	**RBS**	Rutherford Backscattering Spectrometry
EC	Emission Channeling		
FWHM	full width at half maximum	**RBS/C**	Rutherford Backscattering Spectrometry Channeling
GUI	graphical user interface		
IBA	Ion Beam Analysis	**ROI**	region of interest
ISOLDE	Isotope mass Separator On-Line facility	**SBD**	Surface Barrier Detector
		THL	global threshold DAC
IST-CTN	*Campus Tecnológico e Nuclear, Instituto Superior Técnico*	**ToT**	time over threshold
		USB	Universal Serial Bus
		VGA	Van de Graaff accelerator
MCS	Monte Carlo simulation	**ZBL**	Ziegler, Biersack and Littmark

Chapter1

Introduction

1.1   Motivation

In materials science, especially in semiconductor manufacturing, it is important to have a detailed knowledge about the semiconductor's structure resulting from the growing process used.

Rutherford Backscattering Spectrometry Channeling (RBS/C) is an ion beam technique that satisfies several needs of single crystals manufacturers by giving information about the depth profile of the element concentration as well as, due to the channeling information, both crystal quality and impurity lattice location.

Traditional RBS/C is done using careful and well timed step by step line scans. The use of *Position Sensitive Detectors (PSDs)* more importantly than removing the need of angular steps, adds a second dimension to the scan which comes with a significant increase in information.

Solid state *PSDs* for ionizing particles have been used as far back as 1962[1] in a wide range of applications that include high energy physics and medical applications[2]. Timepix[3] is a new type of energy sensitive *PSD*, developed by the Medipix collaboration[4] at the European Organization for Nuclear Research (CERN) in Switzerland. Since Timepix will benefit from finding new applications for this type of PSD, we are also dedicated to reporting our test results to the Medipix collaboration.

Timepix detectors are also a strong candidate for Emission Channeling (EC) at the Isotope mass Separator On-Line facility (ISOLDE) laboratory at the CERN institute. For this reason this thesis also aims at creating the necessary know how, at the home laboratory, for future implementation at ISOLDE.

1.2 Objectives

The main objective of this work, after the obvious master degree conclusion, was to have a working setup with *Timepix* for measuring 2D patterns of RBS/C.

A working setup was established and then used to get a clear understanding of *Timepix* handling and behavior during Rutherford Backscattering Spectrometry (RBS) experiments with He^+. This enabled obtaining quantitative values for energy resolution, angular resolution, effective count rate, optimum bias and radiation hardness, in addition to getting the results of the tested processes for pile-up removal, calibration, data treatment and radiation hardness measurement. It also led to qualitative information about H^+ RBS.

Once the detector operational parameters were established, the following step was to evaluate its performance in real experiments. This was be done by measuring samples of standard substrates and thin films and comparing the analysis to simulations.

The last objective was the writing of this thesis, which will stand as a compilation of the main theoretical baselines for both RBS/C and PSDs together with specific practical information about detector handling and data analysis needed to ensure the reproducibility of the experimental results.

Chapter 2

Theoretical and methodical background

2.1   Rutherford Backscattering Spectrometry (RBS)

Rutherford Backscattering Spectrometry, also know by its initials RBS, is a well established Ion Beam Analysis (IBA) technique for determining the atomic composition of a material, as a function of depth.

The working principle of the method is to target a beam of ions (usually H^+ or He^+) at a sample. The ions interact with the material loosing energy along the traveled path. At the same time, some of the ions have elastic collisions with the target nuclei and are scattered backwards towards the detector with the energy corresponding to the collision kinematics. It is thus only sensitive to elemental composition and not chemical.

The two most common geometries for RBS are the IBM and Cornell geometries described in Figure 2.1. In the figure α is the angle between ingoing beam and normal, β is the angle between outgoing beam and normal and θ the back-scattering angle. In IBM the incident beam, outgoing beam and the surface normal lie within the same plane, therefore $\alpha + \beta + \theta = 180°$. On the other hand, for Cornell it is the rotation axis that makes a plane with the incident and outgoing beam, in this case the relationship between the angles is, $\cos\beta = -\cos\alpha\cos\theta$.

Some of the advantages of RBS are based on the fundamental physics of ion solid interactions which means that there is no need of calibration standards, thus it can be easily associated with other measurements of IBA such as Particle Induced X-ray Emission (PIXE), Particle Induced Gamma Emission (PIGE) and Nuclear Reaction Analysis (NRA). A common complementary and sometimes simultaneous measurement with RBS is PIXE, the first being sensitive to depth and the last being highly
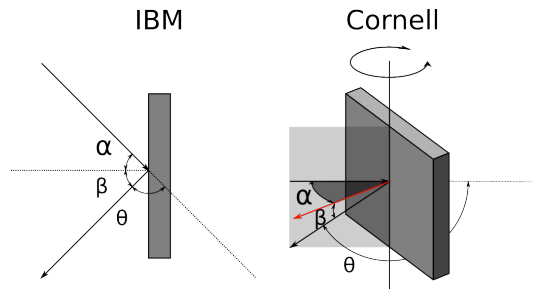
Figure 2.1: IBM and Cornell geometries. α is the angle between ingoing beam and normal, β is the angle between outgoing beam and normal and θ the back-scattering angle. In IBM $\alpha + \beta + \theta = 180°$ while for Cornell $\cos\beta = -\cos\alpha\cos\theta$.

sensitive to composition and stoichiometry.

RBS is also frequently considered as a non destructive measurement in the sense that the mechanical properties and composition of the sample are normally kept. However semiconductor's electrical properties or crystallographic quality can be altered.

RBS is particularly relevant in solid state physics, specially in thin film growth, where it is sometimes necessary to check if the sample composition is the expected one. For this, several spectrometry techniques exist which are usually complementary due to the strengths and weaknesses of each. RBS strengths are to be better suited for retrieving depth information and particularly to measure the concentrations of heavy elements in a light matrix, although it is also sensitive to the rest of the matrix. It can also be used to measure ion implantation profiles, diffusion, surface corrosion, surface roughness, etc.

2.1.1 Physical principles involved

The physical quantities that are used for the spectrum analysis are the energy changes due to the interaction of beam particles with the solid. These are the *kinematic factor* associated with the energy transfer in the collision with a nucleus, the *cross section* that represents the probability of the projectile being backscattered under a certain angle and the *stopping power* that indicates the energy loss according to the path length traveled in the material. All these quantities will be explained with relative detail below together with indications to the bibliographic references[5, 6, 7, 8, 9] for further understanding.

Kinematic factor

Collisions between a beam ion and an atom from the sample are considered to be elastic. Using a classical description, with energy and momentum conservation, it is

4

possible to derive the following relationship between the energy of the incoming ion E_0 and the backscattered E_1

$$E_1 = KE_0, \tag{2.1}$$

where K, the kinematic factor, is given by

$$K = \left(\frac{M_1 \cos \theta + \sqrt{M_2^2 - M_1^2 \sin^2 \theta}}{M_1 + M_2} \right)^2. \tag{2.2}$$

The details of how this equation is deduced are not in the scope of this project and can be consulted if necessary in the references[7, 8].

From equations (2.1) and (2.2) it can be understood that if the beam energy E_0, the ion mass M_1 and the scattering angle θ are known, then there is a direct relation between the measured energy E_1 and the mass of the backscattering atom M_2. As long as we consider only surface scattering.
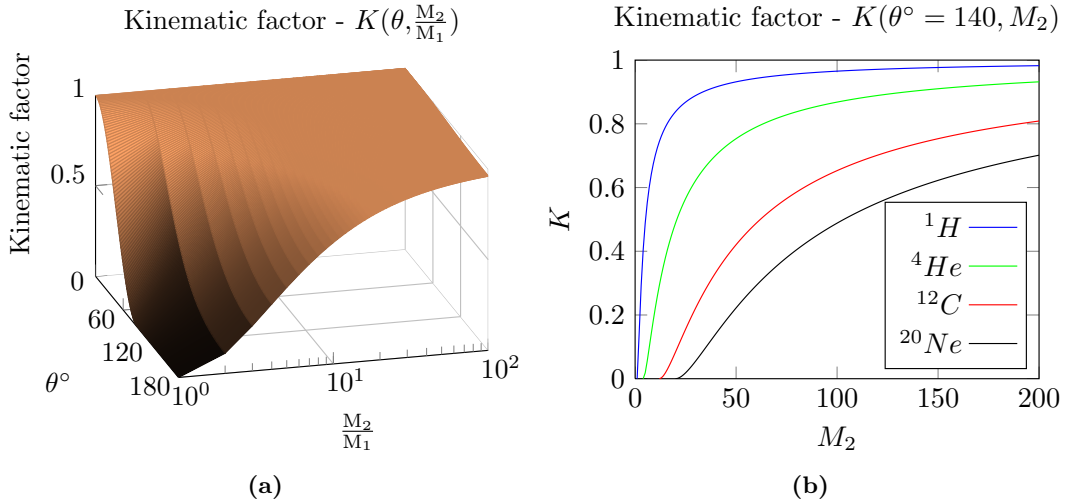
Figure 2.2: Kinematic function visualizations. (a) K as a function of the backscatter angle and the ratio between the two atom masses. (b) K for several beam atoms with $\theta = 140°$ as a function of the mass of the scattering atom.

Figure (2.2) shows two different plots that are useful in giving an understanding of how changes in the geometry or beam atoms can be used to improve mass resolution. Figure (2.2) (a) is a representation of K as a function of the back-scatter angle and mass the ratio between the lattice and beam atom. Figure (2.2) (b) is a representation of K for a given angle of 140° and several beam atoms as a function of lattice atom mass.

The mass resolution is proportional to the derivative of K by the backscattering mass[10]

$$\delta E_1 = E_0 \times \left(\frac{\delta k}{\delta M_2} \right) \times \delta M_2. \tag{2.3}$$

Considering $\theta \approx 180°$ it can be approximated to

$$\delta E_1 \approx E_0 \times \frac{4 M_1 \left(M_2 - M_1 \right)}{\left(M_2 + M_1 \right)^3} \times \delta M_2. \tag{2.4}$$

Furthermore, assuming $M_2 \gg M_1$,

$$\delta E_1 \approx E_0 \times \frac{M_1}{M_2^2} \times \delta M_2. \tag{2.5}$$

From figure (2.2) it is clear that a higher back-scattering angle and heavier beam ions can optimize mass resolution for heavy atoms, such as lower angles (towards 90°) and lighter beam atoms are an optimization for lower masses. Equation (2.5) backs up this idea as it shows that for high atom masses the mass resolution drops with a factor of one over the backscattering mass squared.

One can work around these issues by increasing the beam energy or by using a heavier beam. Although this will bring other complications as with more energetic beams the scattering can be non Rutherford by inducing nuclear reactions. On the other hand heavier beam particles will damage the sample faster.

In general a good compromise is arranged using beams of ^{4}He and $120 \leq \theta \leq 180$.

Rutherford Cross Section

The kinematic factor enables the identification of the backscattering atom, the cross section defines the probability of the scattering occurring at a specific angle. Therefore, it gives information about the concentration of the backscattering atom.
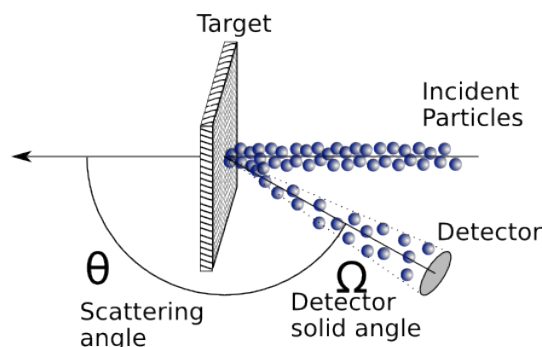
Figure 2.3: Representation of a backscattered beam from an angle θ and subsequent measurement by a detector with solid angle Ω.

Using as general example figure 2.3, where the thickness of the sample is close to zero, the particle density can be converted to a planar density by multiplying the

volume density N by the thickness t. The fraction of the total number of incident particles that scatter into the detector is proportional to the planar density Nt, the angular aperture $d\Omega$ and the differential cross section $\frac{d\sigma(\theta)}{d\Omega}$, therefore obtaining

$$\frac{d\sigma(\theta)}{d\Omega} d\Omega.Nt = \frac{\text{Number of particles scattered into } d\Omega}{\text{Total number of incident particles}}. \tag{2.6}$$

The differential cross section has the dimension of an area and is directly related to the encounter probability of a beam ion with a lattice atom that produces a scattering with angle θ.

The average cross section over the detector surface is therefore

$$\sigma(\theta) = \frac{1}{\Omega} \int_\Omega \frac{d\sigma}{d\Omega} d\Omega. \tag{2.7}$$

The cross section $\sigma(\theta)$ can be derived[8, 7] into

$$\sigma(\theta) = \left(\frac{Z_1 Z_2 e^2}{4E_0}\right)^2 \frac{4}{\sin^4\theta} \frac{\left(\left(1 - [M_1/M_2 \sin\theta]^2\right)^{1/2} + \cos\theta\right)^2}{\left(1 - [M_1/M_2 \sin\theta]^2\right)^{1/2}}, \tag{2.8}$$

with M_1 and Z_1 being the mass and atomic number of the incident ion and M_2 and Z_2 relative to the backscattering atom. This being valid for the laboratory reference.

For $M_1 \ll M_2$ this formula can be expressed as

$$\sigma(\theta) \approx \left(\frac{Z_1 Z_2 e^2}{4\sin^2\left(\frac{\theta}{2}\right) E_0}\right)^2, \tag{2.9}$$

which is the same as if we calculate σ in the center of mass referential.

Several important consequences can be retrieved from equation 2.9. Firstly the cross section goes with the square of Z_1, therefore an experiment with He^{2+} will have twice as much count rate as with H^+. Furthermore it also increases with the square of Z_2 which is an added reason, besides the backscattering energy superposition, for why RBS is a technique more sensitive to heavy elements. It can also be noted that σ increases with $1/E_0^2$ which explains why the backscattering yield increases with the depth of the backscattering as by then the ion has lost a big fraction of its energy.

Non Rutherford Cross Section

There are limitations to the previously explained cross section theory that one must be aware of. Towards low energies the effects of electron screening must be considered by adding during the derivation of the cross section a screening term, usually the Thomas-Fermi function. Low energy correction are mostly useful for surface analysis and therefore will not be further discussed in this thesis, on the other hand high energy

deviations are due to the strong interaction of the ion with the nucleus, in addition to the Coulomb force.

In MeV IBA, it is common to refer the enhancements in the cross sections as, *non Rutherford cross section*. When the incoming particle meets the specific requisites to allow a nuclear reaction with the nucleus the collision will be inelastic and it can even be that the outgoing particle will be from a different type than the incoming. This effect occurs mostly for high beam energies E_0, high scattering angles $\theta \approx 180°$ and low atomic number atoms Z_2.

As in some condition the cross section is greatly increased by this phenomenon, it can be used to enhance sensitivity to lighter elements. Common elements that can be measured with this effect are C, N, O, and Si with [1]p beams above $2.4 MeV$. While for [4]He beams the effect only appears at higher energies as the first resonances is at $3.6 MeV$ for oxygen[5].

Energy Loss - Stopping Power and Straggling

When a fast moving charged particle travels inside a material it will loose energy from collisions and Coulomb interactions with the electrons (electronic stopping) and nucleus (nuclear stopping). The energy loss is dependent from the material and traveling speed.

The knowledge of the energy loss is of great importance for retrieving depth information of the studied sample as the energy difference between particles backscattered at the surface and from within the sample is a function of the depth where the scattering event occurred.

The units used for the energy loss may change with authors but in general the used notation is[11]

$$\epsilon = \frac{1}{N} \cdot \frac{dE}{dx}: \quad eV/\left(atoms/cm^2\right), \qquad (2.10)$$

where ϵ is called the stopping cross section. Remember that here N is the atomic density.

RBS is not sensitive to chemical bonds, only to the individual atoms. This naturally is also applicable to the energy loss, therefore the stopping cross section in compounds can be extrapolated from the known ϵ in pure samples. This method is named *Bragg's rule*. Given a compound $A_m B_n$, with A and B representing the elements and m and n representing the stoichiometric,

$$\epsilon^{A_m B_n} = m\epsilon^A + n\epsilon^B, \qquad (2.11)$$

where ϵ^A and ϵ^B are the cross section of element A and B respectively.

Energy loss is the tool needed for depth profiling, but it comes with a limiting side-effect. Straggling is the energy broadening due to the statistical nature of the energy losses. This means that at the expected energy from a ion backscattered at a surface, most ions will come from the surface depth region, but by looking at the expected energy of a ion backscattered at a deep region an important portion of the ions would have been backscattered from a wider depth region.

Depending on the amount of straggling different theories should be used, as the statistical effect is not always Gaussian, this can be looked in reference[9].

Despite the collisions with electrons there are other sources of straggling, these can be nuclear collisions, geometrical straggling due to finite beam spot size and detector solid angle, multiple small angle scattering and surface or interfaces roughness.

2.2 Rutherford Backscattering Spectrometry Channeling RBS/C

In RBS for amorphous materials the traveling ions suffer random scattering, but this is not always true for crystals. If the beam is set in the direction of one of the crystal's major symmetry axis the ion scattering will be drastically reduced as there will be a "free" path for the ions. An artistic interpretation of the effect can be seen in figure 2.4.
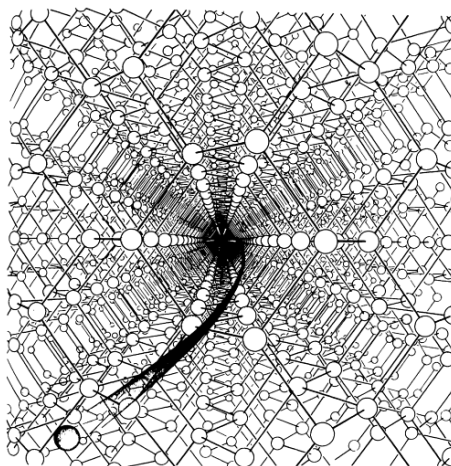
Figure 2.4: Artist interpretation of an ion channeling in a diamond like crystal. From W. Brandt. Copyright © 1968 by Scientific American, Inc. All rights reserved.

As illustrated in figure 2.5, the traveling ions are steered between the crystal's atomic strings which causes a much lower backscattering cross section. To this effect it is given the name of channeling, simultaneously the near absence of traveling ions in the atomic rows is called by blocking. This phenomenon is extremely sensitive

to the matching of the beam with the symmetry axis, therefore the measurements are an angular profile of the cross section between $\approx \pm 3°$ around the main crystal axis. Besides giving the same information as traditional RBS this can also add the crystallographic quality, due to dechanneling from defects or impurities as shown on figure 2.5, lattice location of heavy atoms, structure depth profiling in the case of single-crystalline multilayers and stress between layers.
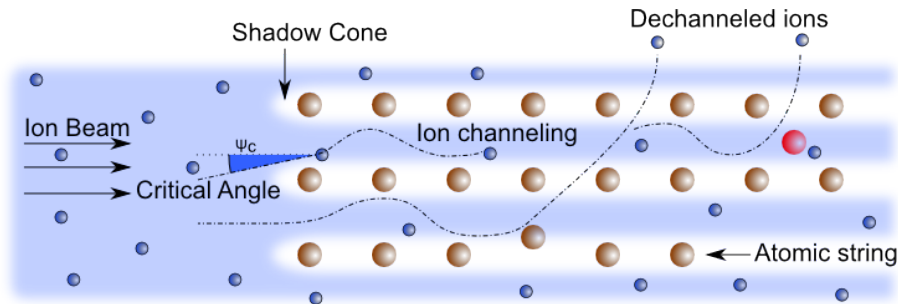
Figure 2.5: Scheme of an ion beam channeled through a crystal. Beam travels in the direction of the arrows. The critical angle is the maximum angle with the surface normal to which channeling still occurs. The shadow cone is a region from which the beam gets deflected at the start of the atomic string. Dechanneling can occur for several reasons, here a displaced atom and an interstitial impurity (red atom) are represented.

2.2.1 Theoretical approaches

In order to gain better qualitative and quantitative insights from the measured data it is necessary to compare them to models. The two best models are the continuum potential approximation from Lindhard[12] which gives analytical formulas for quantities such as the critical angle, and the Monte Carlo simulation (MCS) approach from Barrett[13] using Binary Collision Approximations (BCAs)[14].

Lindhard's Continuum Potential approximation

The steering of energetic atoms along the channeling axis is made by many atoms in which each atom makes only a small contribution in changing the angle of motion, therefore the potential can be approximated by a continuum atomic string.

Lindhard's model uses this approximation to build an analytical description of the channeling effect, which is explained in detail in several books[8, 15, 6]. The Coulomb potential of the atomic string is then

$$U_a\left(r\right) = \frac{1}{d} \int_{-\infty}^{+\infty} V\left(\sqrt{z^2 + r^2}\right) dz, \tag{2.12}$$

where r is the distance from the atomic string, z the axis along the channeling direction, d the distance between atoms in the string along the direction of the channeling and $V(\tilde{r})$ is the screened Coulomb potential with the spherical coordinate $\tilde{r} = \sqrt{z^2 + r^2}$.

For the screened potential a less precise expression than the Molière's is used, but which allows the analytical treatment and is therefore extensively used in channeling theory. The potential is

$$V(\tilde{r}) = Z_1 Z_2 e^2 \left(\frac{1}{\tilde{r}} - \frac{1}{\sqrt{\tilde{r}^2 + C^2 a_{TF}^2}} \right), \tag{2.13}$$

where Z_1 and Z_2 are the atomic charges of the ion and crystal atom respectively, e is the unit charge, $C = \sqrt{3}$, and a is Thomas-Fermi screening distance given by

$$a_{TF} = 0.885 a_0 \left(Z_1^{1/2} + Z_2^{1/2} \right)^{-2/3}, \tag{2.14}$$

with a_0 being the Bohr radius.

From equations 2.12 and 2.13 it is then obtained that

$$U_a(r) = \frac{Z_1 Z_2 e^2}{d} \ln \left(\left(\frac{Ca}{r} \right)^2 + 1 \right). \tag{2.15}$$

Lindhard's equation for the atomic string potential makes possible to derive an equation for the channeling critical angle. For this it is necessary to make a energy description by separating the components of the momentum that are perpendicular $p_\perp$ and parallel $p_\parallel$ to the channeling axis. Which results in

$$E = \frac{p_\perp^2}{2M} + \frac{p_\parallel^2}{2M} + U_a(r). \tag{2.16}$$

Considering a small angle approximation,

$$p_\perp = p \sin \psi \approx p \psi,$$
$$p_\parallel = p \cos \psi \approx p. \tag{2.17}$$

The transverse energy results in

$$E_\perp = \frac{p^2 \psi^2}{2M} + U_a(r). \tag{2.18}$$

Assuming that both the lateral and the lengthwise energies are conserved it is then possible to calculate the critical angle. For this one needs to equate the perpendicular energy at the closest point to the atomic string $U_a(r_{min})$ and at the midpoint between strings $E\psi_c^2$, i.e,

$$E\psi_c^2 = U_a\left(r_{min}\right),$$

$$\psi_c = \left(\frac{U_a\left(r_{min}\right)}{E}\right)^{1/2}. \tag{2.19}$$

The closest point to the atomic string, r_{min}, for derivation purposes, is set by the thermal vibration of the atoms in the string, $r_{min} = \rho$ where ρ^2 is two thirds of the 3-dimensionally averaged thermal vibration mean square amplitude.

Following up equation 2.15, the critical angle can now be said to be

$$\psi_c\left(\rho\right) = \frac{\psi_1}{\sqrt{2}}\left|\ln\left(\left(\frac{Ca}{\rho}\right)^2 + 1\right)\right|^{1/2}, \tag{2.20}$$

with ψ_1, also called by characteristic angle, set as

$$\psi_1 = \left(\frac{2Z_1 Z_2 e^2}{Ed}\right)^{1/2}. \tag{2.21}$$

In an experiment on a given sample the critical angle is then dependent on the beam energy (E), the inter-atomic distance (d), and the temperature $(\rho\left(T\right))$.

The critical angle is one of the most important results from this theoretical description. Another result shows an interesting point in quantification of the difference between the order of magnitude of the channeling and random yield. This can be exemplified on one hand by considering the geometrical limitation of channeling as a circle or radius r_{min} around an atomic string, which is in the order of the $0.01nm$, on the other hand, by limiting the allowed area to πr_{str}^2, with r_{str}, as the radius associated with each string set such that it validates the equation

$$\pi r_{str}^2 = \frac{1}{Nd}, \tag{2.22}$$

which gives that r_{str} is in the $0.1nm$ order of magnitude.

The minimum yield is said to be

$$\chi_{min} = \frac{\pi r_{min}^2}{\pi r_{str}^2}, \tag{2.23}$$

this means that it is around 1% of the random yield.

Barrett's Binary Collision Approximation (BCA)

Barrett made a different approach to the understanding of channeling by using MCS. MCS are a widely used numerical tool in which a large number of essays are made with random initial conditions in order to get statistically valid probabilistic value. In the

case of Rutherford Backscattering Spectrometry Channeling (RBS/C) the output from the simulation is the fluence, of projectiles inside the area of the channel

$$fluence \iff number\ of\ projectiles\ inside\ the\ area\ of\ the\ channel,$$

i.e. the integral over time of the flux, for the same area. With flux defined as

$$flux \iff number\ of\ particles/time.$$

Analytical descriptions allow a deeper understanding of phenomenon but their difficulty increases rapidly with complexity. By doing a numerical analysis Barrett was able to introduce more complexity to the system design, as for example, thermal vibrations. Today, modern programs grant further complexity like impurities and layers.

Barrett's program used a BCA[14, 13], this means that ions will travel in a straight line until an encounter with a lattice atom is made, at the time when a collision is made. Collisions occur in the closest trajectory point of the encountering atom and are instantaneously producing a variation in the ion momentum.

Barrett considered that the thermal vibrations have a Gaussian form according to Debye theory of vibration. The Gaussian expression is

$$F\left(x\right) = \left(2\pi u_1^2\right)^{-1/2} \exp\left(-\frac{1}{2}\frac{x^2}{u_1^2}\right), \tag{2.24}$$

where u_1 is the 1-dimensionally projected root mean square thermal displacement,

$$u_1 = \left\langle x^2 \right\rangle^{1/2} = \left\langle y^2 \right\rangle^{1/2} = \left\langle z^2 \right\rangle^{1/2} \tag{2.25}$$

and is computed from the Debye theory.

The screened potential used by Barrett's calculation was Moliere's[16] approximation to the Thomas-Fermi potential

$$V\left(r\right) = \left(\frac{Z_1 Z_2 e^2}{r}\right) \sum_i \alpha_i \exp\left(-\beta_i \frac{r}{a_F}\right), \tag{2.26}$$

where the Firsov approximation to the screening length, a_F, for completely ionized ions is

$$a_F = 0.885 a_0 Z_2^{-1/3}, \tag{2.27a}$$

or, in case of partially ionized ions,

$$a_F = 0.885 a_0 \left(Z_1^{1/2} + Z_2^{1/2}\right)^{-2/3}. \tag{2.27b}$$

The sum in 2.26 is made with $i = \{1, 2, 3\}$, $a_i = \{0.10, 0.55, 0.35\}$, $\beta_i = \{6.0, 1.2, 0.3\}$ and a_0 is the Bohr radius.

For protons and heavier particles, collisions can be treated classically. In the MCS Barrett used the description made by Lindhard in apendix A of reference[12].

With that, the angle to which the yield falls to half of random is of the form

$$\psi_{1/2} \approx k\sqrt{\frac{V(mu_1)}{E}}, \tag{2.28}$$

where k and m are two constants to be defined. Note that $V(mu_1)$ is the potential close to the limit of the vibrating strings.

Inserting Moliere's potential from equation 2.26 and putting the expression in terms of ψ_1 the equation can be expressed as

$$\psi_{1/2} = k\psi_1 \left[\sum_i \alpha_i \exp\left(-\beta_i \frac{mu_1}{a_F}\right) \right]^{1/2}. \tag{2.29}$$

Using this formula to fit experimentally observed values of $\psi_{1/2}$, the best results found where $k = 0.83$ and $m = 1.2$.

Barrett's empirical formula of the minimum yield is

$$\chi_{min} = 2\pi NdCu_1^2 \left(1 + \left(\frac{\psi_{1/2}d}{ku_1} \right)^2 \right)^{1/2}, \tag{2.30}$$

where he found, by comparison with experimental data, the value of the constants to be $C = 3.0$ and $k = 2.2$. Note that the square root term is near the unity when the energy is in the MeV range, and increases with lower energies.

Monte Carlo simulation programs for ion channeling

Barrett's deduction from his MCS program are a landmark in RBS/C due to the methodology and gained understanding of the phenomenon. Nonetheless, there are nowadays more modern programs which use MCS for understanding the behavior of ion beams in crystals. One such example of these programs is the UT-MARLOWE, developed by Mark T. Robinson[17], which is designed for the simulation of ion implantation in crystals, having therefore to simulate interactions from the entrance of the ion into the crystal until it stops, taking into account multiple scattering events. Another program is the Crystal-TRIM developed by M. Posselt[18, 19], which can simulate implantation of both atomic ions and molecular ions in single crystals of silicon, germanium and diamond with amorphous layers. Finally, the FLUX, developed by P.J.M Smulders[20], is specially developed for channeling phenomena and has been considered as *"excellently suited for lattice location experiments of foreign atoms"[21]*.

More emphasis will be given to the FLUX program as it plays a major role in the development of this thesis.

FLUX is similar to Barrett's MCS programs in the sense that it also uses BCAs but it uses the Ziegler, Biersack and Littmark (ZBL) potential[22] instead, which is given by

$$V_{ZBL}(r) = \left(\frac{Z_1 Z_2 e^2}{r}\right) \sum_i \alpha_i \exp\left(-\beta_i \frac{r}{a_{ZBL}}\right), \qquad (2.31)$$

using as coefficients $\alpha_i = \{0.1818, 0.5099, 0.2802, 0.02817\}$ and $\beta_i = \{3.2, 0.9423, 0.4029, 0.2106\}$. The screening radius a_{ZBL} is

$$a_{ZBL} = \frac{0.8853 a_0}{Z_1^{0.23} + Z_2^{0.23}}. \qquad (2.32)$$

2.2.2 RBS/C with ingoing beam and outgoing beam

Blocking and channeling effects can occur both for incoming and outgoing projectiles, the effect is the same with some differences in energy and geometry.

Lindhard showed in his famous reciprocity theorem[12] that experiments where the ingoing beam of particles is channeled can in principle give the same information as measurements where the outgoing projectiles are blocked. Using a Position Sensitive Detector (PSD), one is obviously interested in the blocking effects of the outgoing particles. The major difference between the two situations is that the incoming projectiles experience channeling at the beam energy but the outgoing ions have the energy corresponding to the beam energy minus the stopping power loss during the inward path and the elastic collision. Lindhard's reciprocity theorem (which is essentially based on time-reversal in classical mechanics) then allows to use MCS programs designed for incoming channeling in order to approximate blocking experiments. For that purpose one assumes an incoming beam with energy equal to the one expected from a detected back-scattered particle. This approach works very well for experimental situations which only probe near-surface depth windows of the sample where energy losses are quite small[21].

Relatively to the geometry, the first difference to notice is that in order to have the incoming beam channeled, a major symmetry axis must be oriented in the beam direction and have a random axis oriented in the detector direction. On the other hand, in order to have the outgoing beam channeled (or blocked) the symmetry axis must be oriented in the detector direction and have in the beam direction a random axis.

Once the channeling direction is found it is then necessary to perform an angular scan around the major symmetry axis. The way to do this for incoming beam channeling is to tilt several times the sample so that there is a different angle between the beam and symmetry axis at each scanning point. For channeling in the outgoing direction the same approach can be used but the tilt will be such that the desired angle is formed between the crystallographic axis and the detector's direction instead. In both situations one usually tries to avoid double alignment, that is, not to have channeling both in the incoming and outgoing directions, as this would complicate the experimental situation. There is yet another option for the outgoing situation, which is to change the angle by moving the detector, this is rarely used as it implies a more complicated setup, but the output is similar to the output produced by PSD, as it will measure several angles without moving the sample.

While it is in principle equivalent to perform RBS/C measurements where the ingoing projectiles or the outgoing projectiles are channeled, there is a big difference regarding the experimental efficiency. In order to measure the backscatter effect from ingoing channeling particles, conventional detectors with relatively large solid angles can be used. If one wants to measure the channeling effect of backscattered particles on their way out of the crystal with a conventional detector, it needs to be collimated to a small solid angle in order to achieve the required angular resolution, drastically reducing the count rate. This does not apply to a PSD, which is able to measure outgoing particles in a wide angular range simultaneously. The fact that no angular scans are then needed during data acquisition greatly simplifies the need for precise sample orientation and charge normalization, thus simplifying the whole experiment.

2.2.3 Applications in Solid state physics

RBS/C is sensitive to any effects that can change the channeling flux distribution. It is therefore advantageous to know what are the expected factors that will induce the dechanneling of ions and consequently flatten the angular distribution or factors that will induce characteristic channeling patterns in certain direction.

Dechanneling even occurs in perfect crystals in the absence of defects, one contribution to this is the electronic scattering. Although a collision of the ion with an electron may not be sufficient to change the trajectory angle above ψ_c, in a many collision path this small-angle scattering can add up and dechannel the ion. Another contribution are thermal vibrations of crystal atoms, which have the direct effect to introduce disorder in the channel potential and therefore have a stronger impact on the dechanneling rate, particularly at high temperatures.

In addition to the effects present in perfect crystals, dechanneling can be induced

by point defects such as missing atoms (vacancies) in the channel walls, atoms which are displaced into or completely interstitial inside the channel, or by extended crystal defects such as dislocations or amorphous regions. Detailed information about dechanneling factors due to different kinds of defects and characteristic channeling patterns can be found in reference[15].

For practical effects, dechanneling will increase the minimum yield by flattening the angular distribution. For this reason the minimum yield is an effective way to get a quantitative analysis of the crystal quality or amount of damage caused by implantation and radiation.

Due to the characteristic energy tag, that identifies the mass of the hit atom, it is possible to measure the channeling distribution of the crystal atoms and impurities separately. This will give insight in the lattice location of the impurity. For example if the backscattering distributions in all symmetry axes have a similar shape for both the lattice and impurity atoms, then it is most likely that the impurity has taken a substitutional location. On the other hand if in some directions there is a peak in the place of the minimum yield this means that in that direction the impurity is in the path of the channeling ions, it is then interstitial[15, 8]. This kind of analysis gives qualitative information on the lattice location. In order to know the exact positions it is necessary to compare with simulations.

Another relevant application is in thin film analysis to measure the elastic strain in epitaxially gown single crystals[23, 24]. Epitaxial growth of a thin crystal on a single crystal substrate will force the growth crystal's lattice to match the existing one. This will cause the planes that are parallel to the surface to have the same lattice parameters $a_\parallel$. What is unknown in this
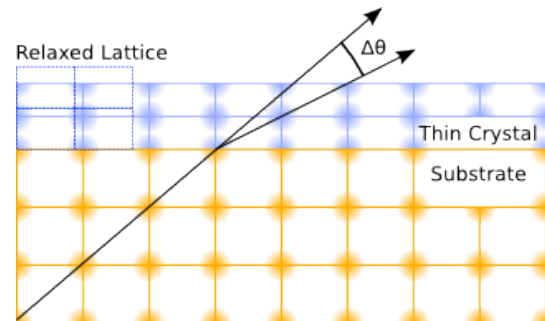
Figure 2.6: Strain channeling visualization

process is the resulting lattice parameter in the planes that are perpendicular $a_\perp$, that due to the Poisson ratio will have a change in dimensions. RBS/C is an effective technique to measure the difference in the lattice parameters by measuring the angular change of the blocking effect between the substrate and the thin crystal. The angular tilt between the channeling from the substrate crystal with lattice constants $a_\parallel$ and $a_{\perp 1}$ and the thin crystal with lattice constants $a_\parallel$ and $a_{\perp 2}$, can be estimated by the following approximation,

$$\Delta\theta = \tan^{-1}\left(\frac{a_{\perp 1}}{a_\parallel}\right) - \tan^{-1}\left(\frac{a_{\perp 2}}{a_\parallel}\right) \approx \frac{a_{\perp 1} - a_{\perp 2}}{2a_\parallel}. \tag{2.33}$$

This formula is accurate when $\Delta\theta$ is bigger than the critical angle, but fails when $\Delta\theta$ becomes of the order of the critical angle or smaller due to an effect called anomalous ion channeling[25, 26] which is explained by the bending of the substrate channeling into the substrate symmetry axes. It is then necessary, for accurate strain measurements to fit the results with simulations.

2.3 Timepix Position Sensitive Detector (PSD)

Timepix[3] are pixelated position sensitive detectors for ionizing radiation developed by the Medipix Collaboration[4] which includes 17 member institutions and is based at CERN, Switzerland. These detectors have the ability to measure simultaneously both the energy and position of the incoming particle.

2.3.1 Sensor, electronic board and readout

Timepix is made by a silicon sensor covered by a thin aluminum layer for bias application (usually 100V) and whose back is connected by bump bonding to an array of 256×256 individual read-out cells that together with the sensor define a pixel. Each read-out is responsible for a set of functions such as the threshold, pre-amplifier, feedback, leakage current and test pulses.

The sensor is made up of a $300\mu m$ thick layer of high resistivity Si which covers an area of $1.5cm \times 1.5cm$ filled with $256 \times 256 pixels$ of $55\mu m$ sides each, as can be seen on figure 2.7.
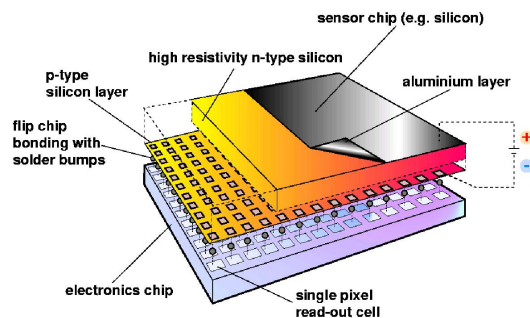
Figure 2.7: Timepix sensor scheme. Image from reference[27].

When a particle interacts with the sensor it creates a charge cloud that is driven by the bias towards the read-out cells where charges are collected. Depending on the deposited energy and bias the charge cloud can be large enough or have time (low bias) to spread to several pixels, an effect which is commonly called charge sharing. Understanding this behavior enables measuring high energy particles without saturation of

the preamplifiers by dividing the charges through several pixels. Also the hit position can be estimated with a position resolution that is smaller than the pixel size if the charge spreads in a Gaussian form, which occurs when the detected particle has only a few MeV.
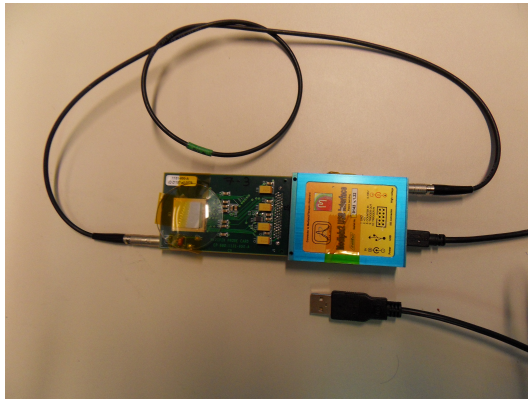
Figure 2.8: Photo of a Timepix connected to the readout Fitpix.

Figure 2.8 shows a photo of a Timepix connected to a read-out system Fitpix[28]. The detector readout is not triggered by particle hits but occurs in regular time intervals, therefore the read-out speed is measure by frame rate instead of count rate. With Fitpix a frame rate up to 90 frames per second is possible.

On each frame there can be several hits that affect several pixels each. The shape of the clusters, that can take several forms, such as a point, Gaussian or track, can be used to identify the radiation type. Hits are then discriminated by considering clusters, groups of adjacent pixels, as hits. Sometimes clusters might be composed by more than one hit, this is an experimental error that one must acknowledge and that is not always easy to remove.

Another nice feature of Fitpix is that it is connected to a computer by a simple Universal Serial Bus (USB). Although the USB can be used to power the chip it is more reliable to use an auxiliary power supply chip which is placed in between of the detector chip and the readout. The power chip must be supplied by a DC source between 3V and 4.5V.

2.3.2 Pixelman

Pixelman[29] is a control and data acquisition software for all the Medipix sensors. The user interacts through a graphical user interface (GUI) that has several functionalities such as to set the device's Digital to Analog Converters (DACs) settings, select the acquisition mode, mask bad pixels, send test pulses for calibration. It also has a plug-in for cluster analysis.

Timepix has tree acquisition modes, medipix mode, timepix mode and time over threshold mode. The medipix mode is not sensitive to energy and counts each pixel activation as one. In the timepix mode the timer starts at a particle hit and stops at the end of the frame. The time over threshold mode, as described in the next section, allows deriving the particle energy by measuring the charge deposited in each pixel, which is digitized and represented as a value between 0 and 11810.

2.3.3 Energy measurement

Timepix measures indirectly the energy of the particle similarly as a Wilkinson Analog to Digital Converter (ADC). The deposited charge is used to charge a capacitor and the discharge is made at a constant current, the deposited charge can then known by the timing the *time over threshold (ToT)*. Figure 2.9 is a representation of this process, each color line corresponds to a different deposited energy and corresponding charge, higher charges (red) stay longer above the threshold (black horizontal line) than lower charges (blue). The DAC that controls the discharge current is the IKRUM.
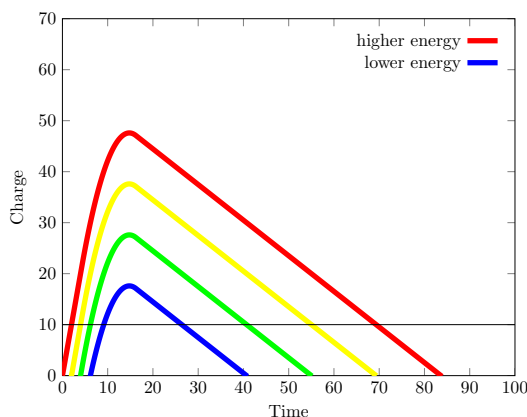
Figure 2.9: Representation of the charge vs time in a pixel. The black horizontal line corresponds to the threshold.

Setting the threshold just above the noise prevents the events from being caused by noise. Timepix is then able to measure radiation from tens of keV to tens of MeV. Energies above $\sim 1MeV$, however, can only be measured if saturation of preamplifiers is avoided by exploiting charge sharing between pixels.

As pixel characteristics are not the same all over the detector, such as the leakage current, preamplifier gain and the effective threshold (function of the set threshold and the feedback), each pixel needs to have its threshold equalized and have an individual calibration.

The function that relates the energy with the ToT is a surrogate function, defined by

$$ToT(E) = a \times E + b - \frac{c}{E - t}. \tag{2.34}$$

and can be visualized in figure 2.10.

For a full chip calibration it is therefore needed to define $4 * 256 * 256 = 131072$ parameters.
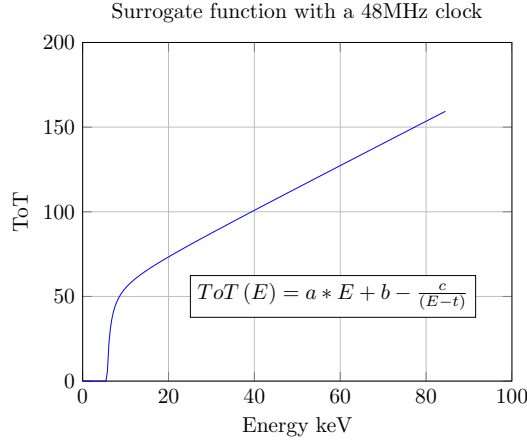
Figure 2.10: Graphical representation of the surrogate function in which values are as expected by Timepix measurements.

2.4 Resistive charge division Position Sensitive Detector (PSD) for Rutherford Backscattering Spectrometry (RBS)

As it is in the scope of this thesis to write a comparison between the studied timepix and the previously studied[30] resistive charge division PSD, this short section will introduce this type of PSD. The referred PSD has a surface of $10 \times 10\text{mm}^2$, a thickness of 300μm and achieved a position resolution of 0.19mm as well as an energy resolution of 33keV.

A resistive charge division PSD is a Si diode where the front and back planes consist of resistive n- and p-type layers which have two linear metal contacts x1,x2 (front) and y1,y2 (back) deposited on opposite sides, as shown in figure 2.11.

The energy signal in this type of detector is obtained by adding the the collected charges, either from the front or back side:

$$\begin{aligned} E_{front} &= E_{x1} + E_{x2}; \\ E_{back} &= E_{y1} + E_{y2}. \end{aligned} \tag{2.35}$$

2.4. RESISTIVE CHARGE DIVISION Position Sensitive Detector (PSD) FOR Rutherford Backscattering Spectrometry (RBS)
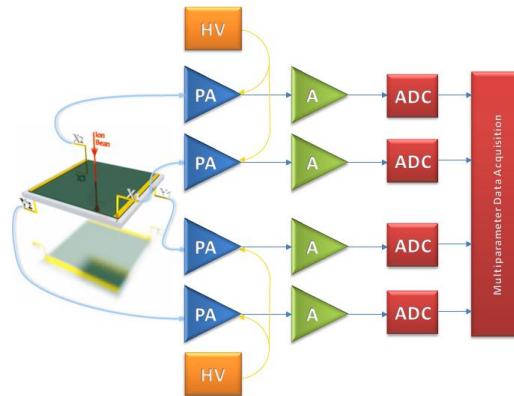
Figure 2.11: Schematics of a resistive charge division PSD and respective read-out system. HV - High Voltage; PA - Pre-Amplifier; A - Amplifier. Image from reference[30]

The front and back plane of the detector behave as linear resistors, where the charge collected on the electrodes is divided proportional to the coordinates of the particle impact point. The position signals x and y are hence obtained according to

$$
\begin{aligned}
\frac{x}{L} &= \frac{E_{x1}}{E_{x1} + E_{x2}} \\
\frac{y}{L} &= \frac{E_{y1}}{E_{y1} + E_{y2}}
\end{aligned}
, \tag{2.36}
$$

were L is the side length of the detector.

Whereas such detectors have been used in a variety of cases for emission channeling experiments using radioactive alpha emitters [31], their use for RBS/C is a novelty. Figure 2.12 shows RBS/C result from an early stage development of a resistive charge division PSD.
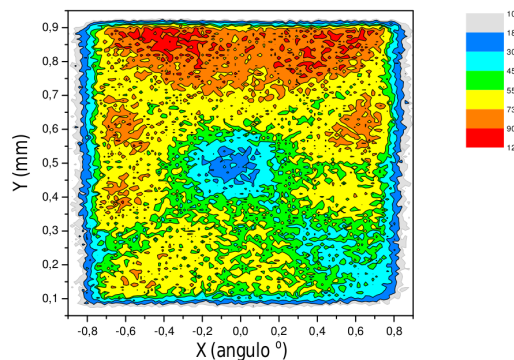
Figure 2.12: Rutherford Backscattering Spectrometry Channeling (RBS/C) of a silicon sample. Figure from reference[30].

Chapter3

Methodology

The previous chapter presented the motivation for performing this work and put it into the proper scientific and technologically relevant context.

In the present chapter this knowledge is developed into applications by introducing the equipments, software and samples used.

3.1 Equipment setup and geometry

The experiment used the Van de Graaff accelerator (VGA) existing at the *Campus Tecnológico e Nuclear, Instituto Superior Técnico* (IST-CTN). A representation of the beam setup can be seen in the schematics of figure 3.1.

The accelerator can produce beams of He$^+$ and H$^+$ with energies up to 2.5MeV although for stability purposes it is preferable to stay at 2.0MeV.
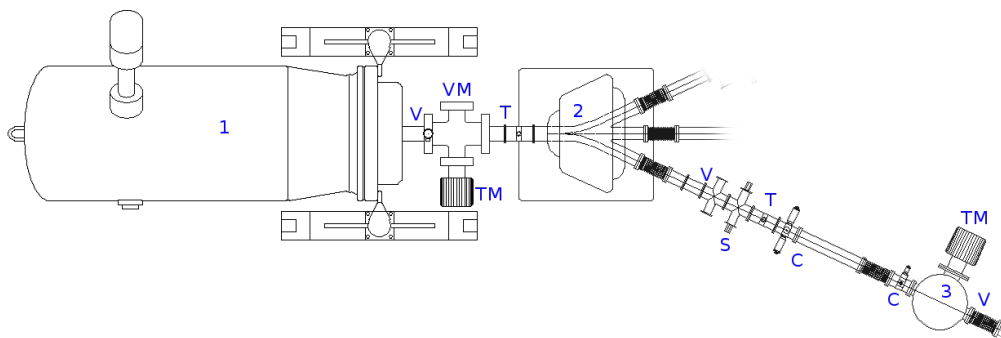
Figure 3.1: Schematics of the Van de Graaff accelerator (VGA) setup in IST-CTN. 1 – Van de Graaff accelerator (VGA); 2 – magnet 25° (deflector); 3 – Experiments chamber; V – Vacuum valves; TM – Turbomolecular pump; S – Stabilizing slits; C – beam collimators; VM – Manometer; T – beam interceptor. Schematics adapted from reference [32].

During operation of Rutherford Backscattering Spectrometry (RBS) experiments in the chamber (figure 3.1:3) the magnet selects the energy of the beam particles that are deflected into the chamber (figure 3.1:2) and the accelerator voltage balanced automatically so that the current that passes between the slits is optimized.

The two-axis goniometer in the chamber (figure 3.1:3) allows to rotate the sample in the beam and detector plane (polar angle θ) and around the axis defined by the sample surface normal (azimuthal angle φ). Thus it follows the IBM configuration, see figure2.1. This allows the orientation of the sample symmetry axis in the desired direction.

Some specifications important to note for the Rutherford Backscattering Spectrometry Channeling (RBS/C) experiments are the beam energy spread $\leq$ 5keV and the goniometer angular precision $\Delta\theta \approx \pm 0.02°$ and $\Delta\varphi \approx \pm 0.04°$. Additionally, there is a known deviation in the beam energy to lower energies that has not been fully characterized, its value stands in the range of 0 to 50keV.

The beam arrives in the chamber through a $0.5mm$ collimator, leading to a beam spot size of 0.5(+0.1) mm, at an angle of 140° to the detector, with the sample as vertex.

3.2 Detector usage

The detector is attached to the experimental chamber (number 3 in figure 3.1) at a 40° degree angle to the beam entrance. It stands at a distance of $192mm$ from the sample holder and has a surface of $15mm \times 15mm$ with an angular aperture of 4.46° degree. A photography of the mounting can be seen in figure 3.2.

The detector power supply comes from a home made 220V AC to 4V DC converter that connects to a voltage stabilizer chip plug between the readout FITPix and the detector. The readout is then connected to the PC by USB. The high voltage supply for the bias is embedded in FITPix and is controlled by Pixelman.

In order to block the pixel readout from noise events but without loosing detection capabilities an individual threshold must be set to each pixel by a 4-bits Digital to Analog Converter (DAC). Pixelman's plug in for equalization sets a threshold correction to each pixel by measuring the noise center with the correction DAC set to its maximum and afterwards set to its minimum. The noise center is measured by scanning the number of counts in medipix mode as a function of the global threshold DAC (THL). The histogram of all pixels noise center will be Gaussian shaped. The equalization is concluded by interpolating the maximum and minimum pixel correction with the noise center, so that the pixel correction and THL are set to the point where the THL is at
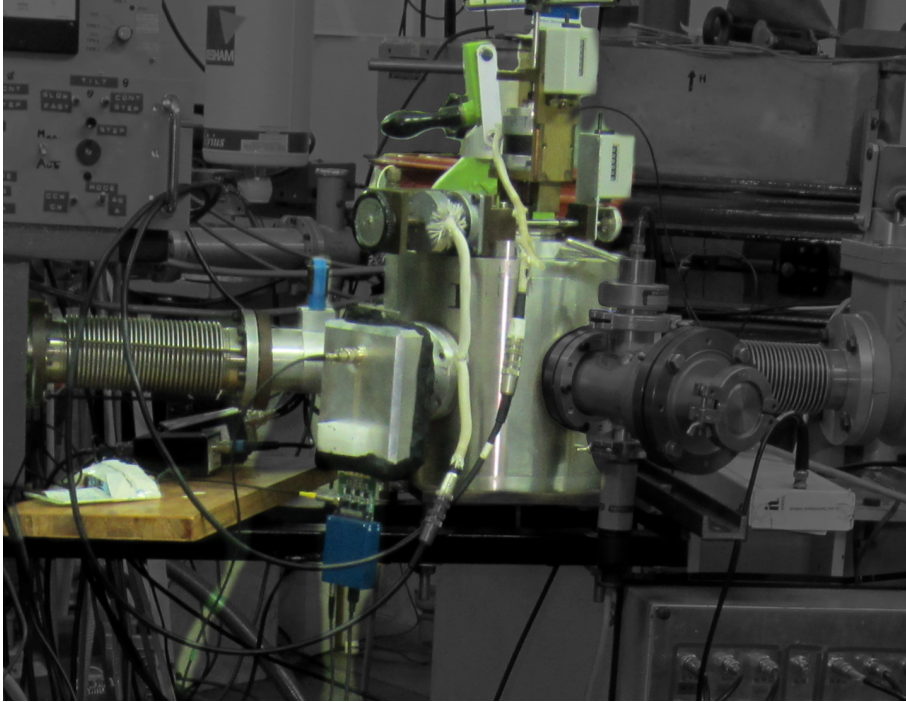
Figure 3.2: Photography of mounting of the detector at the experimental chamber. To the detector, the power regulator chip and Fitpix (blue box) are connected.

the noise center of each pixel. After equalization the noise center histogram results in a much sharper histogram.

After this procedure the THL must be adjusted by at least 40 DAC levels so that the threshold stays above noise.

Masked pixels are set by sending 100 test pulses to each pixel, in medipix mode, and each pixel that records a count significantly different than 100 is considered either noisy or dead and therefore masked.

3.2.1 Test Pulse calibration

In section 2.3.3 it was described how Timepix is sensitive to energy. In order to carry out the calibration one needs to inject the charge that can be related to a certain amount of energy. One way to do this is by irradiating the detector with X-rays of well known energies and of a wide range of energies as described in reference [33]. A more practical way, that can be done with the detector in the experimental chamber, is by using internal test pulses.

Most of the requirements for calibration come from the fact that each pixel has its own preamplifier and Analog to Digital Converter (ADC), with each one having slightly different responses. This means that we need to do a per pixel calibration, i.e. we need 256x256 calibration curves. Electronic test pulses send voltages between 0.0V

and 0.5V with a 1mV step to each pixel through the capacitor located right before the readout cell, as indicated in figure 3.3.
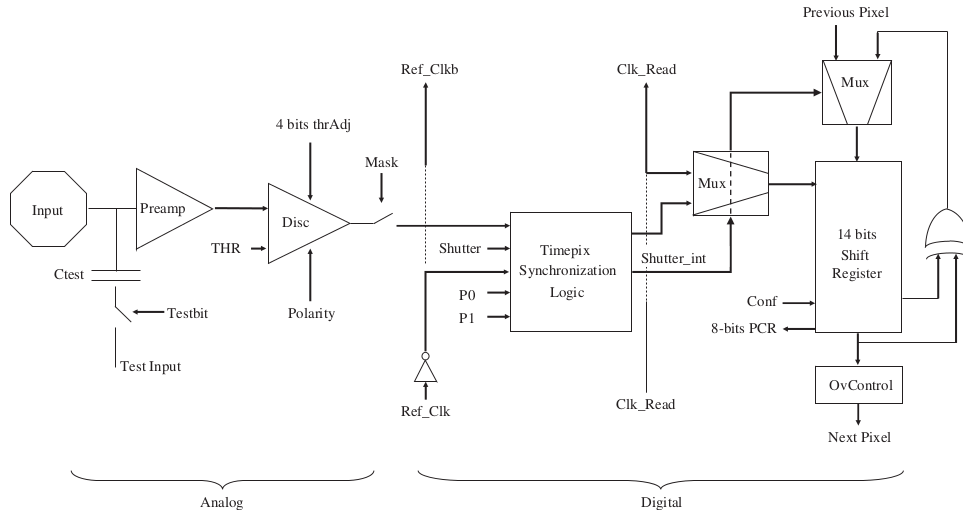
Figure 3.3: Schematic representation of the electronic cell for each pixel. Figure from reference [3].

A relationship between the test pulse voltage and the equivalent energy can be established. For this it is necessary to determine how much charge was injected into the preamplifier, which will be the charge correspondent to approximately 82.5% of the capacitor

$$Q = \frac{\alpha V_{TP} C_{Test}}{q}, \tag{3.1}$$

where $\alpha = 0.825$ is the fraction of the capacitor charged, V_{TP} is the test pulse voltage, C_{test} is the capacitor charge of $8fF$ and q is the electron charge.

A second requirement is to determine how much charge is created in the silicon when energy is deposited by a ionizing particle. To do this, one electron-hole pair liberated is counted for each 3.6eV deposited,

$$E = Q \times 3.6eV \tag{3.2}$$

The resulting relation is

$$E = \frac{3.6\alpha C_{Test}}{q} V_{TP}. \tag{3.3}$$

This corresponds to $148500eV$ for each V. A more precise relation has been simulated for the capacitor input gain[3]. The resulting value was that 1V of test pulse is equivalent to $169687.5eV$, this was the equivalence used.

After the test pulse response is recorded a fit of parameters a, b, c and t, is then made with the surrogate equation

$$ToT(E) = \begin{cases} a.E + b - \frac{c}{E-t} & if\ E \geqslant \lambda, \\ 0 & if\ E < \lambda, \end{cases} \qquad (3.4)$$

where λ, the root of the surrogate function, is defined by

$$\lambda = \frac{\sqrt{a^2t^2 + 2abt + 4ac + b^2} + at - b}{2a}. \qquad (3.5)$$

Note that for energies $E \gg c + t$ the surrogate function approaches a simple linear response with an offset b.

The fit routine used is the TMINUIT, from the root framework developed at CERN, embedded in a C++ program RedPix developed by Ligia Amorim and maintained by myself.

3.2.2   Data acquisition

Data is recorded by Pixelman's cluster analysis plug-in in a text file. Each line corresponds to a cluster where each activated pixel is recorded by three numbers in the following way $[X\ Y\ ToT]$. X and Y are the vertical and horizontal position, ranging from 0 to 255 and time over threshold (ToT) is the time over threshold ranging from 0 to 11810, that can then be converted to energy by the inverse of the surrogate function, $ToT^{-1}(E)$.

One problem that this method creates is that the Gaussian charge distribution resulting from alpha particle detection may be cut in half by dead pixels. This propagates the error of the dead pixels to its neighbors as one cluster cut in half, will be counted as two alpha particles of lower energies, as exemplified in figure 3.4.
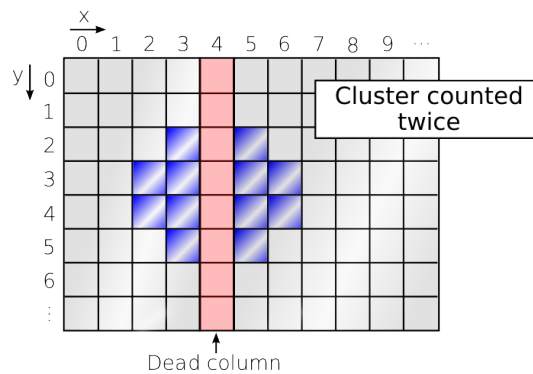

Figure 3.4: Example of a cluster divided by dead pixels.

3.3 Data treatment with Redpix

RedPix, the C++ program developed for the data treatment, has two principal embedded data structures. One is a 3D histogram, the *timepix matrix,* that is a 3D matrix in which two indices represent each pixel X and Y position and the third index is the energy bin number. Each matrix value stores the number of counts that corresponds to the defined energy range and X and Y position.

The other data structure is a 2D histogram, the *medipix matrix*, that is a 2D matrix whose two indices refer to X and Y positions only. The stored value is an integral of the counts in the timepix matrix over a user defined energy range. The medipix matrix does not necessarily need to be used for histograms as it can also store test pulse ToT response or calibration parameter results.

First step with RedPix is to load each test pulse file to a medipix matrix and do a calibration fit. The initial values used for the fit are $a = 1.5$, $b = 35$, $c = 10$ and $t = 5$ and the initial errors are $\Delta a = 10$, $\Delta b = 20$, $\Delta c = 40$ and $\Delta t = 10$. The number of loop steps is 20, this takes around 20min to fit.

After the fit is made and calibration parameters stored in disk, one can load the experimental data into a timepix matrix. For this it is necessary to input the range of energies to record and the number of bin for the timepix matrix. During the data reading process the cluster pixels are converted from ToT to energy and the cluster centroid and volume are calculated. The bin that corresponds to the position and energy of the cluster is then incremented by one.

Energy histograms are made by integrating over the requested pixels. 2D channeling patterns are made by integrating the timepix matrix of a given range of bins, and creating a medipix matrix.

3.4 RBS simulation program - SIMNRA

SIMNRA[34] is a spectrum simulation and fit program for RBS. It was used with the backscattering spectrum of the measurements, to fit the calibration parameters, the number of particles per solid angle unit and the composition and thickness of the layers.

The calculation options used included: isotopes, straggling, multiple scattering and double scattering, stopping power data from SRIM [22], energy loss and straggling model from Chu and screening to Rutherford cross section model from Andersen.

The energy region of interest (ROI), corresponding to the desired depth range for channeling simulation, was also calculated by SIMNRA. This was accomplished by simulating a backscattering spectrum in the same conditions as the experiment but

with a sample only as thick as the depth ROI then recording the energy at half height of the top and lower slopes.

3.5   FLUX for RBS channeling simulation

In order to perform FLUX simulations two input files are needed, one that defines the sample crystal structure and layers which is called "COMBI4.FIG", and an other, that defines the simulation conditions, called by input file (extension ".inp"). The way that each of the files is written is complicated because the program used, developed in 1987, focused in memory saving above practicality. The full procedure is too extensive to be explained in this text (above 20 pages). Therefore only the physical parameters that need to be used will be described here and reference [35] is suggested for tutorials on writing the input files.

In order to define a new structure in the "COMBI4.FIG", one must define a crystal unit cell in which channeling occurs in the Z direction and for which the full crystal can be created by translational or mirror symmetries. The structure description includes the existing atomic species, number of atoms and lattice constants. Besides the unit cell structure, surrounding rows that will be accounted for by the continuum potential approximation, are also defined, these are added by inserting their X and Y positions. For the atoms in positions that are qualified for binary collisions besides the X Y coordinates the position in Z must also be detailed.

The input file must include a tag for the desired structure previously detailed in COMBI4.FIG. It must also include several other types of information, such as:

- The number of layers (1 for single crystals);
- The number of constituents in the host lattice;
- The nuclear charge and mass of both the ions and lattice atoms;
- The Debye temperature;
- The initial channeling energy (the beam energy for ingoing channeling and the backscattered energy for outgoing channeling);
- Coordinates of initial ion position (usually a random generated flat distribution that covers the whole entrance of the unit cell);
- The sign of the energy loss (positive for ingoing beam RBS/C and negative for outgoing beam RBS/C);
- Energy dependent stopping due to the valence electrons;
- Energy dependent stopping due to collisions with the inner shells electrons;
- Depth distribution of backscattering particles (uniform for host lattice atoms and Gaussian for implanted impurities);
- Energy dependent cross section for the host and impurity atoms;

- Beam standard deviation for ingoing beam RBS/C or standard deviation of angular resolution due to beam spot size and detector resolution for outgoing beam RBS/C;
- Maximum permitted angle with beam direction during scattering events;
- Number of tracks to simulate;
- List of all the angles to simulate (in a 128×128 matrix these are 16384 angles).

With these two files as input FLUX will perform Monte Carlo simulation (MCS) in each angular direction in order to create a flux distribution along the channel for each depth step. Ions that get out of the channel will be taken into account in the normalization by being added as a flat background.

In order to get the atom and lattice position specific 2D patterns as measured with the position sensitive detectors, it is necessary to integrate over a circular area centered in the desired lattice position with radius of the desired atom mean squared lattice vibration. In this way, each simulated FLUX distribution will give a value for one point in the 2D pattern.

For a reliable quantitative analysis the simulated 2D close-encounter probability distribution pattern, χ_{theo}, must be compared with the experimental 2D count histogram, χ_{exp}. This is done by using the Levenberg-Marquardt[36] algorithm to iteratively reduce the value of the following expression,

$$\chi^2 = \left[\frac{\chi_{exp}(\theta, \varphi)}{S} - [f\chi_{theo}(\theta', \varphi' + \varphi_0) + (1 - f)] \right]^2, \tag{3.6}$$

in which the parameters that are allowed to vary are the S, f, φ_0 and (x_0, y_0) in $\theta'(x_0, y_0)$ and $\varphi'(x_0, y_0)$. The φ_0 and (x_0, y_0) are the offsets needed so that the simulation orientation matches the one of the detector, S is a normalization parameter for the experimental results, f is fraction of the measured pattern that can be matched by the simulation and consequently $(1 - f)$ is the random fraction, in other words, the fraction of which is a flat distribution.

3.6 Samples

In this section the different samples that were used during the experiments are going to be described, including relevant characteristics for the simulations.

In Ion Beam Analysis (IBA) it is usual to express the thickness in $particles/cm^2$, or in angstrom Å. For practical conversion between these two units, the density of each material in this section will be described in $particles/\left(cm^2 Å\right)$.

The first sample used was a alpha radioactive source with three isotopes, ^{239}Pu, ^{241}Am and ^{244}Cm, with an activity of $< 1\mu$Ci. The principal alpha emission energies for ^{239}Pu, ^{241}Am and ^{244}Cm are 5.145MeV, 5.486MeV and 5.804MeV respectively.

An amorphous sample of thin films was used in RBS. Its composition[37] was C/SiO$_2$/Au, in which the carbon is the substrate, the silicon oxide has a 760Å thickness and the gold thickness is of 170Å. The carbon particle density is $10,037 \times 10^{14} particles/ \left(cm^2 Å\right)$, the silicon oxide particle density is $5.218 \times 10^{14} particles/ \left(cm^2 Å\right)$ and the gold density is $5.900 \times 10^{14} particles/ \left(cm^2 Å\right)$.

The single crystals used were:

1. Silicon that has a diamond cubic structure, Debye temperature of 498K [38] and a particle density of $4.995 \times 10^{14} particles/ \left(cm^2 Å\right)$. Silicon was used for the purpose that single crystals are reproducibly available in very good quality, and it is well established that FLUX works extremely accurate in predicting channeling effects in that material. This is documented in the literature by the fact that the Si Debye temperature derived from comparing FLUX results to experimental RBS/C energy spectra is 490K, in accordance with other methods [39]. This Debye temperature, corresponding to a thermal vibration amplitude of 0.0825Å at 20°C, was therefore also used here. For the purpose of comparison between samples the energy loss in silicon for a 2MeV He ion is of 23.33eV/Å.

2. For 6H silicon carbide the particle density is $9.6419 \times 10^{14} particles/ \left(cm^2 Å\right)$. As for the room temperature thermal vibration amplitude, differing values are reported in the literature. Ref. [40] reports for 4H-SiC $u_1\left(Si\right) = u_1\left(C\right) = $ 0.0696Å, which would correspond to $T_D\left(Si\right) = 590$K and $T_D\left(C\right) = 966$K, and Ref. [41] for 2H-SiC $u_1\left(Si\right) = 0.0603$Å, $u_1\left(C\right) = 0.0611$Å, corresponding to $T_D\left(Si\right) = 692$K and $T_D\left(C\right) = 1142$K. On the other hand, some sources, e.g.[42], quote for all polytypes of SiC Debye temperatures around $1200\cdots1300$K. The energy loss in silicon carbide for a 2MeV He ion is of 36.15eV/Å.

3. Strontium titanate that has an perovskite structure and the particle density is $7.892 \times 10^{14} particles/ \left(cm^2 Å\right)$ and the energy loss for a 2MeV He ion is of 40.57eV/Å.

Chapter4

Results and discussion

The measurements and results shown in this section are the principal milestones concerning the detector implementation as stipulated in the objectives detailed in chapter 1. This will follow the logical sequence by first defining the detector energy sensitivity, second defining the angular resolution by fitting with 2D patterns, then continuing by verifying with other crystals for eventual improvement of details on fitting strategies, and finally by real-life applications on sample characterization.

4.1   Triple alpha source energy detection

The triple alpha source using the isotopes ^{239}Pu, ^{241}Am and ^{244}Cm was the ideal start for testing the detector and software due to limited beam time availability, having a stable setup only used by this experiment and lower risk of detector damage due to the low sample activity.

Several trials where made to optimize the Digital to Analog Converter (DAC) parameters, as the leakage current controller (IKrum), which was set to 5, and the change in threshold (THL) after equalization, which is reduced till all pixels are no longer triggered by noise instead of masking the ones with more noise, about 40 DAC levels. Simultaneously bugs in RedPix where fixed and test pulse calibration optimized till the one described in the methodology.

The resulting energy histogram, presented in figure 4.1, brings into conclusion that the energy accuracy is under 50keV and the energy resolution of 90keV FWHM at the energy of the ^{241}Am alpha emission peak, 5.486MeV.
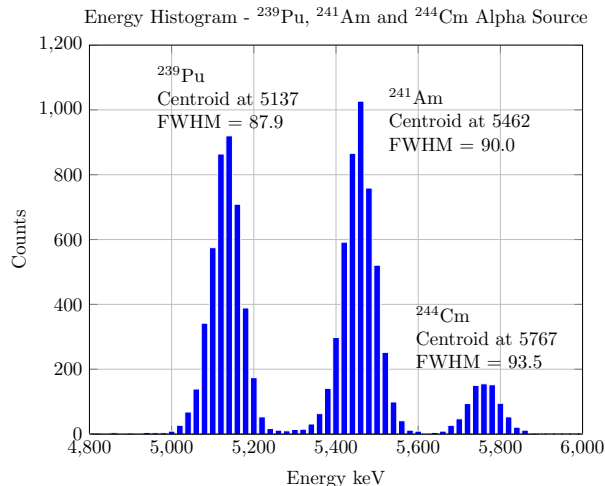
Figure 4.1: Energy histogram from the triple alpha source. Positions of Gaussian fit centroids and FWHM are indicated in order to evaluate the detector energy accuracy and resolution.

4.2 Amorphous thin film analysis with 2MeV Helium beam

Although the 5MeV region alpha source was practical for the first developments, the energy 5-6MeV energy regime is out of range of application in 2MeV Rutherford Backscattering Spectrometry (RBS). For this reason the calibration was made using the Au thin film in the sample of $Au/SiO_2/C$, described in section 3.6, for which, due to its low thickness, has a natural width of only 28keV for backscattered 2MeV alphas. In addition, the irradiated sample produce a high count rate due to Au high cross section.

The plot in figure 4.2 was obtained with a 2MeV beam, with the detector operating at a frame rate of 0.05s and bias of 25V. The bias was reduced from the usual 100V to allow charge spread between pixels, and secondly was optimized for energy resolution.

The measured energy histogram was simulated and fitted by SIMNRA to obtain the best energy calibration. The obtained conversion from the measured energy by Timepix E_{TP} to the expected from SIMNRA simulation E_{Calib} was

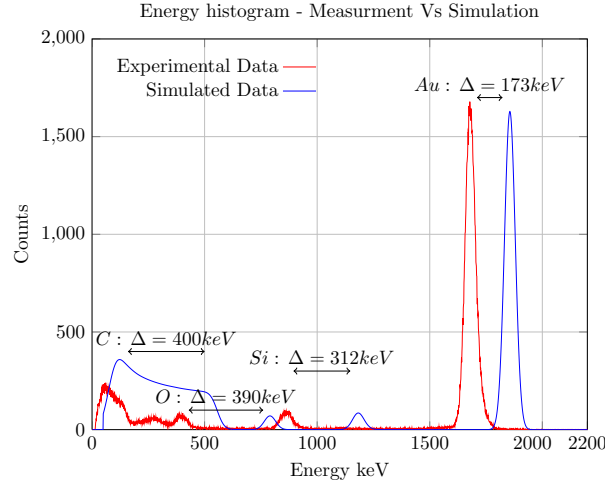$$E_{Calib} = 459 + 0.83 \times E_{TP}. \tag{4.1}$$

Figure 4.2: Helium backscattered energy spectrum of the Au/SiO$_2$/C sample at a 2MeV beam. Comparison between Timepix detected energy and the expected energy from simulation with SIMNRA.

There are two things to notice on graph 4.2, the Gaussian FWHM and the offset from close to 200keV at the gold peak and reaching 400keV at lower energies. The gold peak kinematics suggests that the detected energy at this geometry should be of 1862keV. An explanation which can, at least partially, explain such shifts is a relatively thick detector entrance window, as will be discussed in section 4.5.1.

The solution found for the fast degradation of the energy accuracy at lower energies, validating the data for Rutherford Backscattering Spectrometry Channeling (RBS/C) experiments, was to use the calibration set in equation 4.1. This equation had to be slightly adapted for other spectra using the surface step in the energy spectrum as a reference. The surface step occurs at a characteristic energy from ions backscattered at the surface, it can be easily identified in the RBS energy spectrum.

The measured FWHM of 54.9keV can be corrected for the natural width of the Au peak, which for a 2MeV He ion is expected to be of 28keV. To correction to the energy resolution can be made as follows,

$$FWHM_{measured} = \sqrt{FWHM_{detector\,resolution}^2 + FWHM_{natural}^2} \qquad (4.2)$$

$$FWHM_{detector\,resolution} = \sqrt{54.9^2 - 28^2} = 47.2 \qquad (4.3)$$

this corresponds to an energy resolution for Timepix of 47.2keV. In comparison, a standard Surface Barrier Detector (SBD) used in the same facility had a Au peak FWHM of 30.8keV.

4.3 Amorphous thin film analysis with 2MeV proton beam

The response of the Timepix detector was also tested on RBS with hydrogen beam as this kind of beams is sometimes used to detect lighter atoms by using their resonance properties and still keep the beam under 2MeV.

Figure 4.3 shows the fitted spectrum backscattered hydrogen in the Au/SiO$_2$/C sample. This spectrum was obtained with geometry defined by an entrance angle of 30°, exit angle of 10° and backscattering angle 140°. The measurement had a duration of 1h with a 5nA beam current, with the detector operating at a frame time of 0.05s and bias of 25V.
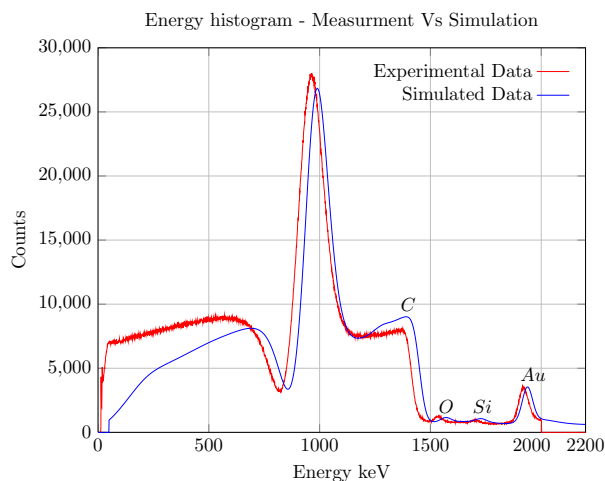
Figure 4.3: Hydrogen backscattered energy spectrum of the Au/SiO$_2$/C sample at a 2MeV beam. Comparison between Timepix detected energy and the expected energy from simulation with SIMNRA.

During the fitting the beam energy was also corrected, and 1970keV was used instead of 2000keV.

For the hydrogen the gold peak FWHM is of 54keV, which by taking into account of the peak 7keV natural FWHM results in a energy resolution 53.5keV, close to the one for the helium beam.

The hydrogen measurement results in a much more accurate energy detection, having only a 15keV offset for the gold peak. As will be discussed in section 4.5.1 this is due to protons having a lower energy loss while traveling in the detector top layer.

4.4 Single crystal measurements

The single crystals measured are samples of good quality and with properties broadly known in the scientific community. This made it easier to associate findings to the detecting system. The first crystal measured was silicon (Si) because it is the most broadly used semiconductor, is easy to obtain with high quality and was previously analyzed by a resistive charge Position Sensitive Detector (PSD). Other measured crystal were the silicon carbide (6H-SiC) because it was also compared with the PSD and strontium titanate ($SrTiO_3$) because it is a compound of three distinguishable atomic masses.

4.4.1 Silicon, Si

The silicon sample was measured during a total of 6 hours with an average beam current of 9nA. In order to measure the <100> direction, the geometry in the IBM configuration was set at a backscattering angle of 139.5° and at an entrance angle of 40.5°.

The spectrum was analyzed with the calibration that resulted from the $Au/SiO_2/C$ sample analysis, with a small correction so that the surface energy fit the simulated spectrum. This kind of offset, of a few keV, is expectable, as it may depend on the detector threshold, which is defined at the beginning of each experiment. The calibration was used to select the events corresponding to a backscattering depth range of $0 \longmapsto 2000$Å which, by its turn, according with SIMNRA simulations, corresponds to a energy range of $1204 \longmapsto 1092$keV.
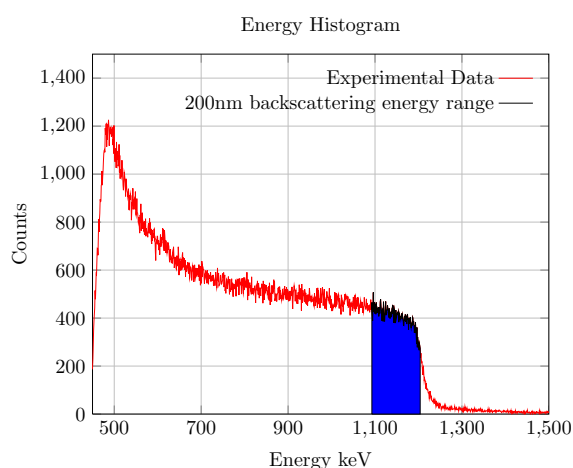

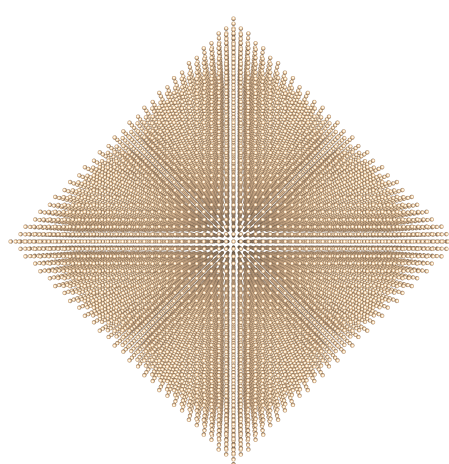**Figure 4.4:** Energy histogram of $^4He^+$ backscattered in Si, with 2000Å depth highlighted energy range.

Figure 4.5: Graphical representation of a Si crystal in the <100> direction.

The <100> direction of the crystal is set towards the detector. A representation of what is seen by the detector is shown in figure 4.5. At the center of the image is the <100> channeling effect, on the horizontal and vertical directions are the major planes (110) and on the diagonals are the minor planes (100). All this can be easily identified in the resulting 2D histogram patterns.

For the selected energy range, a 2D histogram is made and normalized to its integral. This can then be fitted with FLUX simulations as shown in figure 4.6.
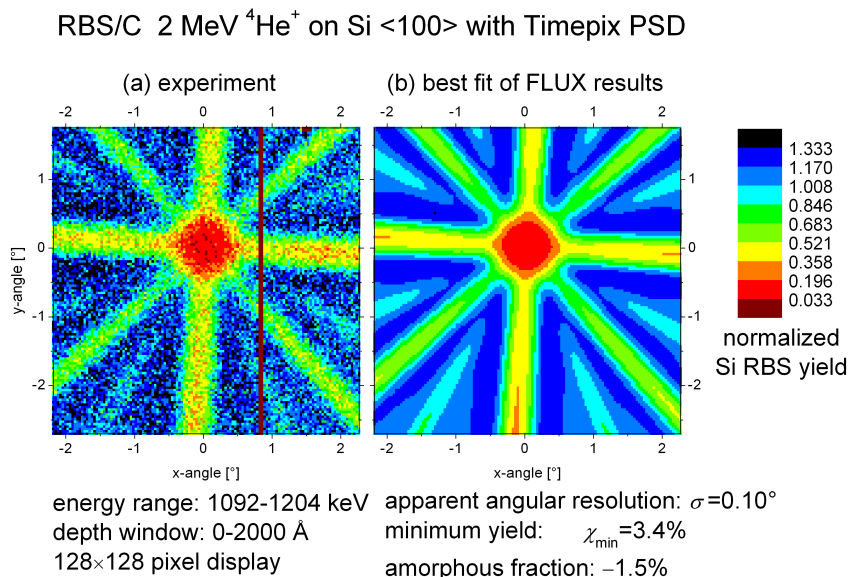
Figure 4.6: Normalized 2D patterns for silicon in the <100> direction. The patterns bins are reduced from 256 to 128 for better visualization. a) The normalized pattern for the data in the referred depth range, measured with Timepix. b) FLUX pattern that better fits the data.

The fit result from figure 4.6 shows that for the several essays with different angular resolutions, the resulting best fit is for an angular resolution of $\sigma = 0.10°$. This gives a resulting minimum yield of $\chi_{min} = 3.4\%$ and an amorphous fraction of -1.5%. Therefore one can conclude that the measured crystal is close to perfect. The reason for the negative fraction is that in the center of the channel statistics are too low for an accurate error calculation.

As a comparison, the same sample was measured by a resistive charge PSD, as shown in figure 4.7. The difference in visible details can be appreciated by looking at the patterns. Moreover, quantitative analysis shows that the angular resolution is twice as much as that of the pixel detector. The minimum yield measured with the resistive charge detector is inaccurate as the poorer angular resolution flattens channeling in the axis direction. The result is an angular resolution for the detector of $\sigma = 0.2°$. The sample has a minimum yield of $\chi_{min} = 18.5\%$ and an amorphous fraction of 5.7%.

RBS/C 2 MeV ^{4}He$^+$ on Si <100> with resistive charge PSD

(a) experiment   (b) best fit of FLUX results

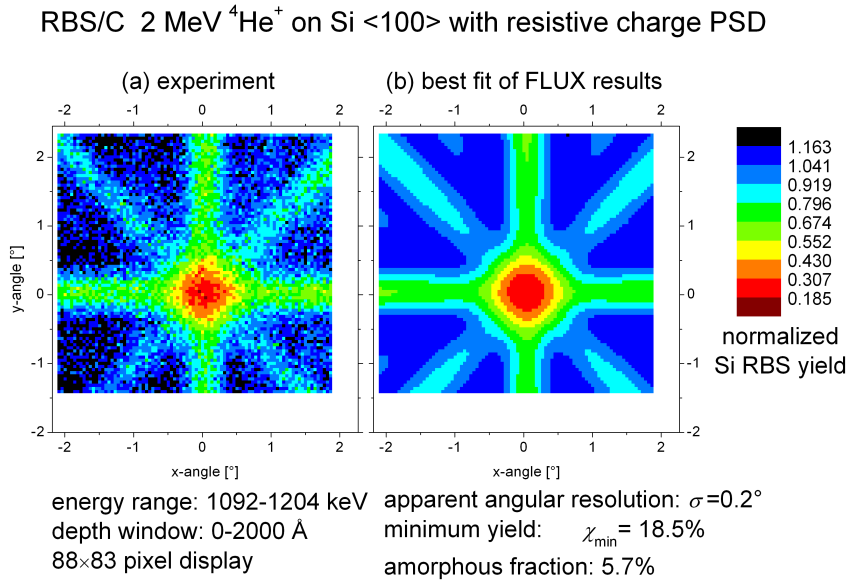energy range: 1092-1204 keV   apparent angular resolution: σ=0.2°
depth window: 0-2000 Å   minimum yield: χ_{min}= 18.5%
88×83 pixel display   amorphous fraction: 5.7%

Figure 4.7: Normalized 2D patterns for silicon in the <100> direction. a) The normalized pattern for the data in the referred depth range, measured with a resistive charge PSD. b) FLUX pattern that better fits the data.

The achieved angular resolution, resulting from the combination of beam spot size, distance of detector to sample, and position resolution of the detector, was assessed by comparing the experimentally determined channeling effects from a Si <100> sample in the depth range $0 \longmapsto 2000$Å to a set of simulated patterns which were calculated using FLUX for a wide range of angular resolutions.

The energy of the ^{4}He projectiles in the simulation was assumed to be 1.204MeV, corresponding to the backscatter energy from the surface of a Si target. The simulations were performed for an angular range of +-3° from the <100> with a step width of 0.05°. The angular resolutions (standard deviation σ) considered ranged from 0.04° to 0.40° in steps of 0.01°.

4.4.2 Silicon Carbide, 6H-SiC

The 6H-SiC sample is a step forward in the testing of the detector's response as it has two different atom masses and the Debye temperature for the FLUX simulations was uncertain.

In order to measure the [0001] direction, the geometry in the IBM configuration was set at a backscattering angle of 139.5° and at an entrance angle of 40.5°.

As with the silicon sample a $0 \longmapsto 2000$Å depth range was chosen having as reference the Au/SiO$_2$/C calibration, which according to SIMNRA simulations, corre-

sponds to a energy range of $1204 \longmapsto 1037\text{keV}$ for the backscattered $^4\text{He}^+$ in Si and $587 \longmapsto 428\text{keV}$ when backscattered by C atoms. As can be seen in figure 4.8, C backscattered particles are mixed with Si backscattered particles from higher depth regions making them unqualified for fitting. The energy region of interest (ROI) for 6H-SiC is slightly larger than for the Si, despite the depth range being equal, due to its higher stopping power.
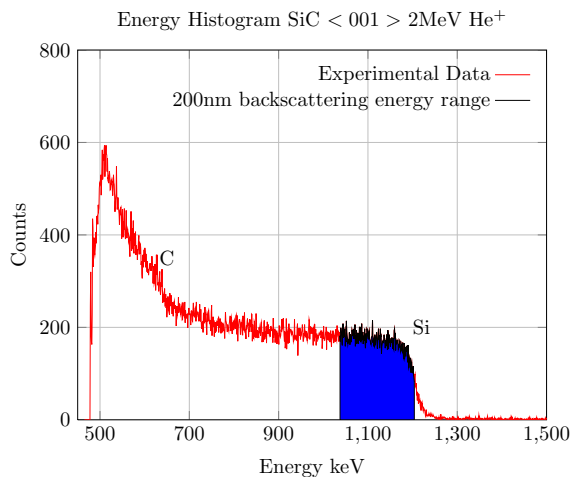

Figure 4.8: Energy histogram of $^4\text{He}^+$ backscattered in 6H-SiC, with a 2000Å highlighted energy range for Si backscattered $^4\text{He}^+$.
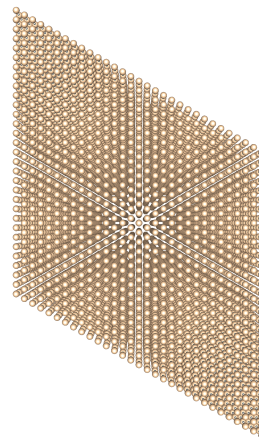
Figure 4.9: Graphical representation of a 6H-SiC crystal in the [0001] direction.

Figure 4.9 is a representation of a 6H-SiC crystal in the measured [0001] direction. Here one can clearly see the same 60° rotation symmetry, with a strong axis in the center, as in the analysis 2D patterns.

Since the literature describes different values for the thermal vibrations in SiC, it was decided to compare experimental RBS/C data on [0001] 6H-SiC to a set of FLUX simulations using six different Debye temperatures ranging from $T_D(Si) = 590\text{K}$, $T_D(C) = 966K$ to $T_D(Si) = 1010\text{K}$, $T_D(C) = 1542\text{K}$ in steps of 100K.

The energy and angular range of the simulations were chosen as in the case of Si.

The resulting pattern and FLUX results from the Timepix measurement can be seen in figure 4.10. The best fit to the experiment was obtained for $T_D(Si) = 707\text{K}$ and $T_D(C) = 1080\text{K}$, close to the values reported by Ref. [41], for an angular resolution of $\sigma = 0.12°$, in reasonable agreement with the angular resolution determined from Si <100>. This results in a minimum yield of 4.5% and an amorphous fraction of -0.2%.

As with the silicon sample, counts in the center of the channel are very low, meaning that some pixels got zero counts. This affects the fit as its error is unknown.

One thing to notice is the anisotropy in the random count rates in different positions

RBS/C 2 MeV ^{4}He$^+$ on 6H-SiC [0001] with Timepix PSD
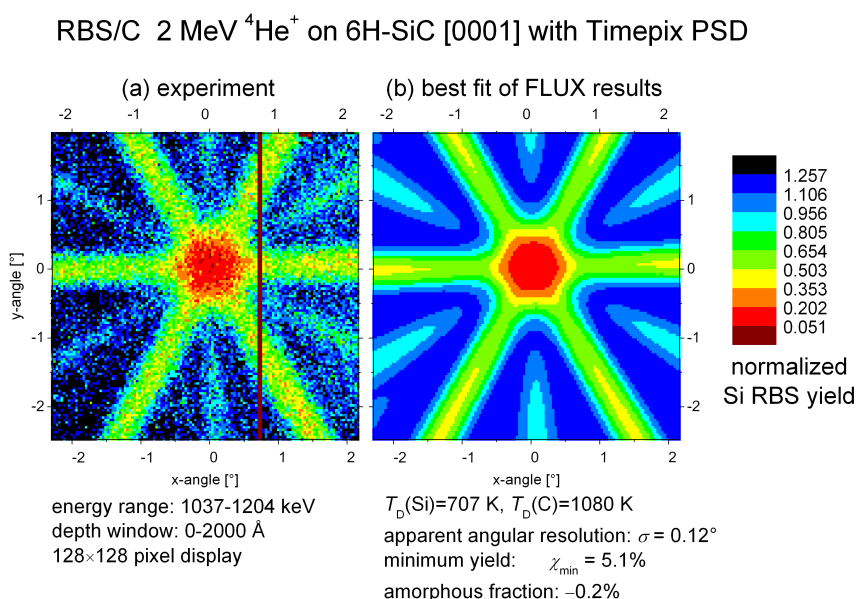
Figure 4.10: Normalized 2D pattern of a Timepix measurement for 6H-SiC crystal in the [0001] direction.

of the detector, that are more pronounced in the case of 6H-SiC measurements than in the case of Si. This is due to the energy calibration having different offsets in these places, therefore when selecting the ROI, areas where the surface energy is higher will have more events and areas where the surface energy is lower will have fewer events.

RBS/C 2 MeV ^{4}He$^+$ on 6H-SiC [0001] with resistive charge division PSD
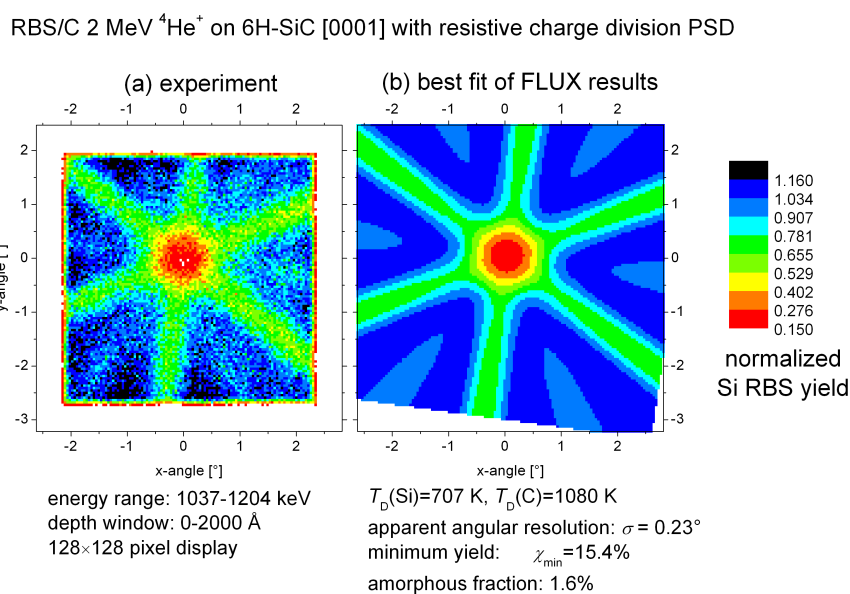

Figure 4.11: Normalized 2D pattern of a Resistive Charge PSD measurement for 6H-SiC crystal in the [0001] direction.

This same sample was measured with a resistive charge detector in order to see the differences. Figure 4.11 shows the comparison. A clear improvement of Timepix is the visibility of the minor places and the hexagonal shape of the channel. Fit results shows a factor of two improvement of the Timepix's angular resolution $\sigma = 0.12°$ over the resistive charge PSD's with $\sigma = 0.23°$. The minimum yield also shows a significant difference from $\chi_{min} = 4.5\%$ for Timepix to $\chi_{min} = 15.4\%$ for the resistive charge PSD.

4.4.3 Strontium Titanate, SrTiO₃

This section is intended to show the feasibility in measuring a set of directions for a given crystal. Figure 4.12 compiles the measurements of SrTiO$_3$ made with Timepix. From sub-figure a) to d) different crystal orientations are shown. The major and minor planes are visible in the representation and can also be identified in the measured 2D patterns in sub-figures f), g) and h). The random orientation is present in all measurements in the flat regions away from the axis and planes.

For measuring the crystallographic quality by the minimum yield the best axis is usually the <100> as the channeling effect is stronger. For the measurement of some crystallographic properties, such as, lattice location or elastic strain, it may be necessary to measure channeling along several axis.

Measurements were done with a beam current of 4nA and had an acquisition time of 3h for the <100> direction, 1h30 for the <211> direction and 3h for the <111> direction.

It is then shown here that different symmetry axes can be measured for complementary information. The were only three minor difficulties found in the process being one, that the patterns can't be seen in real time as there is always the delay from data transfer and analysis present. Two, that low statistics makes it hard to identify correctly the planes so each orientation step needs to accumulate enough statistics to make a move in the correct direction. The last difficulty is that with the two degrees of freedom goniometer it was not always trivial to center the symmetry axis in the detector vertical plane.

(a) SrTiO$_3$ in a random orientation.

(b) SrTiO$_3$ viewed from the <100> direction.

(c) SrTiO$_3$ viewed from the <111> direction.

(d) SrTiO$_3$ viewed from the <211> direction.

(e) Energy Histogram with highlighted Sr 200nm energy ROI.

(f) 2D pattern in the <100> direction.

(g) 2D pattern in the <111> direction.

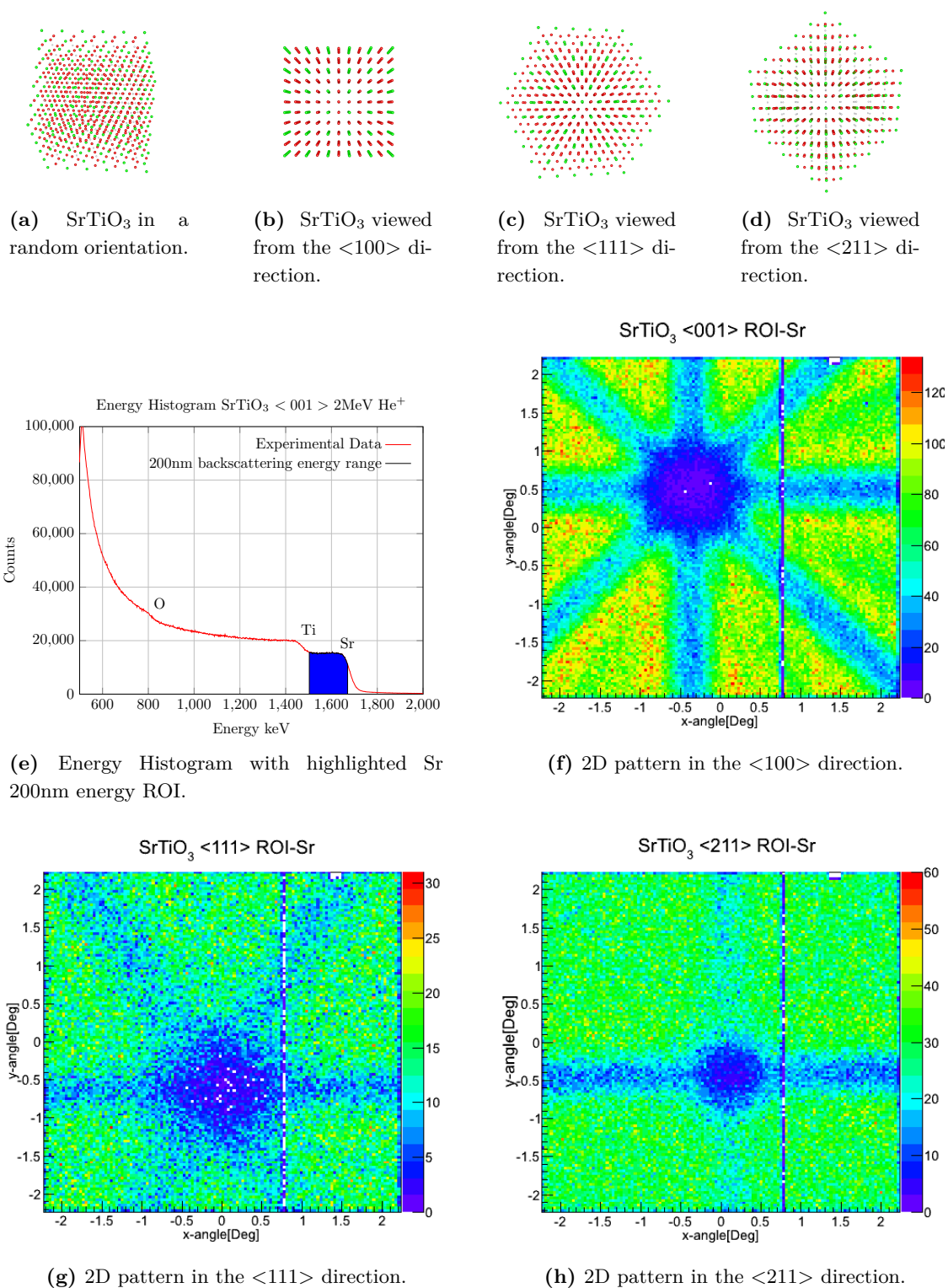**(h)** 2D pattern in the <211> direction.

Figure 4.12: SrTiO$_3$ crystal visualization with respective measured energy histogram and 2D patterns.

43

4.5 Timepix characterization

The set of experiments carried out enabled the characterization of Timepix for experimental relevant factors. These include the energy resolution, the setup overall angular resolution, the effective count rate and the radiation hardness.

4.5.1 Energy resolution and accuracy

The $Au/SiO_2/C$ thin film measurement with helium beam discussed previously shows an energy resolution of 45keV at 1862keV and an offset of closely 200keV increasing at lower energies to values above 400 keV. In order to explain this shift a hypothesis will be presented in the following, although it can be proven not to be sufficient on its own.

The first thing to notice is that the offset is not the same for the whole chip. Using the same data as shown in figure 4.2, a 2D distribution of the Au backscattered energy centroid along the detector's surface was made as can be seen in figure 4.13. Each bin is a average of the centroid over 8×8 pixels.
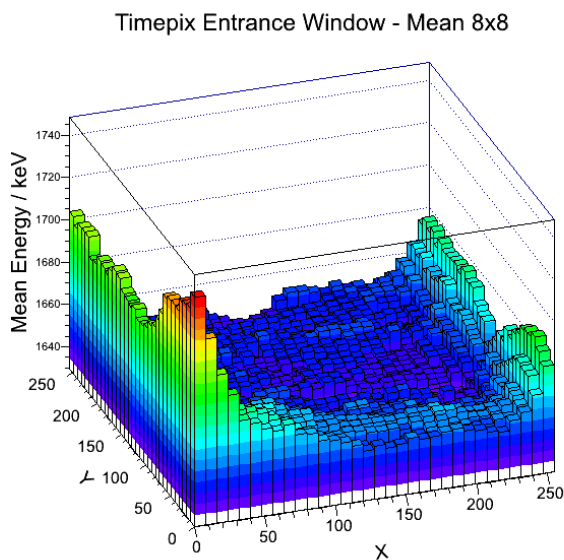
Figure 4.13: 2D distribution of Au backscattered energy centroid along the detector's surface. A concave shape is found in the center of the detector.

The test pulse calibration does not take into account any effect that may occur before the charge enters into the readout circuits through the bump bonds. This means that there can be several contributions that are ignored during the calibration, and that become only relevant at low energies as this shift has not been reported at higher energies by experiments made by other members of the Medipix collaboration.

The main hypothesis that is presented here, is that the thin aluminum layer existing on the surface of the detector (see figure 2.7) is, at least partially, responsible for the energy loss of the detected alpha particles. Using the SRIM software to obtain the energy loss for helium ions traveling in aluminum, it can be calculated that the thickness required to cause an energy loss of 173keV for a 1862keV helium beam is 622nm. Additionally the same thickness calculation can be made for an energy loss of 312keV for a 1180keV beam resulting in 1198nm, and 1206nm for a loss of 390keV for a 790keV beam. This suggests that the Al thickness should be 622nm or less and that probably also other factors are responsible for the offset at lower energies, which we have to leave as an open question.

This is backed-up by the fact that little energy shifts where found for the hydrogen backscattering particles, which at this energy range have a stopping power one order of magnitude lower than helium.

4.5.2 Position resolution, overall angular resolution,

The effective angular resolution is a combination of the position resolution of the detector and the beam spot size. The detector position resolution for alpha particles is unknown; previous measurements of a scan over 1×2pixels with a short pulse LASER to simulate alpha particles where able to determine the Gaussian centroid with a precision of 1μm[43]. Such a high precision is in practice is not possible as it would require a much higher count rate, in addition, the bad quality energy calibration results in non-Gaussian energy clusters.

From the angular resolution standard deviation of $\sim 0.11°$and the distance from the sample to the detector of 192mm, the position resolution standard deviation can be calculated by

$$\Delta X = \tan\left(\Delta\theta\right) \times 192\text{mm} = 0.37\text{mm}. \tag{4.4}$$

Which is around the size of the beam spot, or seven pixels. Therefore the angular resolution is well above the capacity of the detector and could be improved with a smaller collimator. On the other hand, a smaller collimator will mean lower count rate and more damage, as the beam incidence would be more focused.

4.5.3 Pile-up and cluster size

The nature of the hit particle is identified in Timepix by the cluster shape, X-rays give single or double pixel clusters, beta particles leave scattering tracks and alphas Gaussian clusters. When two particles hit nearby pixels within the same time frame,

the two events may combine into a single cluster, the result is loss of Gaussian shape and the addition of the two particle energies. This effect is knows as pile-up.

During RBS/C experiments, in the low energy region Timepix detects both X-rays and alpha particles. These can be hard to distinguish, therefore only clusters with more than 3 pixels are used for the analysis. This induces a cutoff at the low energies in the histograms that has no physical meaning.

One could also set an upper range for cluster sizes in order to remove pileup. Although, this could remove clusters of sizes that are only possible with pile-up, as there is no specific size at which single hits stop and pile-up starts this would also remove some clusters that do not correspond to pileup. Doing this also results in changes in the shape of the energy histogram and reduces the quality of simulation fitting, as SIMNRA can take pile-up into account during simulations but only if it was not changed by a cluster size limitation. In conclusion a lower limit was set at 3 pixel clusters but no upper limit was established.

4.5.4 Effective count rate

In order to reduce the pileup it was then necessary to either reduce the ^{4}He beam current or increase the frame rate. Fitpix can achieve a frame rate of 90 frames per second with a frame time of 0.001s. Since this corresponds to a live time of 0.09s/1s, this means 91% dead time during which the detector is busy with readout but the sample and detector will keep receiving damage from the beam. As best compromise for this situation we chose a rate of 15 frames per second with 0.05s frame time, corresponding to 25% dead time. At this frame rate and with beams of ~ 20nA it was possible to achieve a count rate around ~ 2kHz with relatively low pile-up.

4.5.5 Radiation hardness

In the course of these experiments a significant amount of radiation was directed to the detector. This usually creates defects in the semiconductor that act as charge traps causing changes in the energy resolution and in the depletion of the semiconductor, especially when working at low bias voltages.

The integrated fluence received by the detector was estimated to be 7.5×10^7particles/cm^2 which produced no detectable changes in the energy resolution.

Chapter5

Conclusions

This research in experimental physics reports a sequence of steps for the setup and evaluation of the Timepix pixelized detectors for Rutherford Backscattering Spectrometry Channeling (RBS/C) experiments. More specifically, it compiles the required knowledge for the operation of the detector as well as the analysis of measurement data, together with experimental results for the quantification of the detector characteristics.

RBS/C is an ion beam technique for structural analysis of single crystals which enables the measurement of several characteristics, such as, crystallographic quality, lattice location of impurities and elastic strain.

The methodology used for the calibration included as a first step the injection of internal test pulses followed by fitting the surrogate function response using the ROOT TMINUIT library inserted in a C++ program RedPix. This was followed by fitting real RBS energy spectra using the SIMNRA code. Angular blocking patterns were analyzed by means of comparing to simulated patterns using the FLUX code.

Optimized bias for measurements at 2MeV was found to be 25V.

The measurement of the backscattering helium in the gold thin film led to the conclusion that the energy resolution of the detector is 45.6keV at 1862keV.

An energy loss was detected that in the best of our understanding is due to an aluminum layer on the surface of the detector.

Using a sample-detector distance of 192mm and a beam spot of 0.5mm an angular resolution of 0.11° was reached.

The effective count rate achieved was 2kHz. Higher count rates can be realized but only at the cost of additional pile-up. Increasing the frame rate is not a viable option since it implies longer dead time for the detector.

No radiation damage effect on energy resolution was found at a fluence of 7.5×10^7 particles/cm^2.

Blocking patterns were measured for single crystals of silicon, silicon carbide and strontium titanate, which enabled a verification of the crystallographic quality of the first two.

Future work from this project includes the simulation of $SrTiO_3$ with FLUX, the elastic strain analysis of thin InAlN films deposited on GaN, measurement of the gold film with a new detector that doesn't have an aluminum layer on top, calibration improvement with data analysis by numerical tools and a graphical user interface (GUI) for building "COMBI4.FIG" structures for FLUX.

Bibliography

[1] K. Lauterjung, J. Pokar, B. Schimmer, and R. Stäudner, "Grenzschichtzaehler fuer orts- und energiebestimmung," *Nuclear Instruments and Methods*, vol. 22, pp. 117–121, Mar. 1963.

[2] E. Lægsgaard, "Position-sensitve semiconductor detectors," *Nuclear Instruments and Methods*, vol. 162, pp. 93–111, Jan.

[3] X. Llopart, R. Ballabriga, M. Campbell, L. Tlustos, and W. Wong, "Timepix, a 65k programmable pixel readout chip for arrival time, energy and/or photon counting measurements," *Nuclear Instruments and Methods in Physics Research Section A: Accelerators, Spectrometers, Detectors and Associated Equipment*, vol. 581, pp. 485–494, Oct. 2007.

[4] M. Campbell, "10 years of the medipix2 collaboration," *Nuclear Instruments and Methods in Physics Research Section A: Accelerators, Spectrometers, Detectors and Associated Equipment*, vol. 633, Supplement 1, pp. S1–S10, May 2011.

[5] H. R. Verma, *Atomic and Nuclear Analytical Methods: XRF, Mèossbauer, XPS, NAA and Ion-beam Spectroscopic Techniques.* Springer, 2007.

[6] G. Schatz and A. Weidinger, *Nuclear condensed matter physics: nuclear methods and applications.* Chichester; New York: John Wiley, 1996.

[7] W.-K. Chu, J. W. Mayer, and M.-A. Nicolet, *Backscattering spectrometry.* Academic Press, 1978.

[8] T. L. Alford, L. C. Feldman, and J. W. Mayer, *Fundamentals of Nanoscale Film Analysis.* Springer, 2007 ed., Feb. 2007.

[9] M. Mayer, "Rutherford backscattering spectrometry (RBS)," May 2003.

[10] Rui Manuel Coelho da Silva, *Estudo por RBS e canalização iónica de ligas de Mg, Al e Fe formadas por implantação iónica.* PhD thesis, Faculdade de Ciências da Universidade de Lisboa, Lisboa, 1993.

[11] T. L. Alford, L. C. Feldman, and J. W. Mayer, *Fundamentals of Nanoscale Film Analysis.* Springer, 2007 ed., Feb. 2007.

[12] J. Lindhard, *Influence of Crystal lattice on motion of energetic charged particles.* bind 34, nr. 14, Kobenhavn Kommissionaer: Matematisk-fysiske Meddelelser, 1965.

[13] J. H. Barrett, "Monte carlo channeling calculations," *Physical Review B*, vol. 3, pp. 1527–1547, Mar. 1971.

[14] M. T. Robinson, "The binary collision approximation: Background and introduction," *Radiation Effects and Defects in Solids*, vol. null, no. 1, pp. 3–20, 1994.

[15] L. C. Feldman, *Materials Analysis by Ion Channeling: Submicron Crystallography.* Academic Press, Nov. 1982.

[16] G. Molière, "Therorie der streuung schneller geladener teilchen i. einzelstreuung am abgeschirmten coulomb-feld," *Z.Naturforsch*, vol. 2a, p. 133, 1947.

[17] M. T. Robinson and I. M. Torrens, "Computer simulation of atomic-displacement cascades in solids in the binary-collision approximation," *Physical Review B*, vol. 9, pp. 5008–5024, June 1974.

[18] M. Posselt, "Crystal-trim and its application to investigations on channeling effects during ion implantation," *Radiation Effects and Defects in Solids*, vol. null, no. 1, pp. 87–119, 1994.

[19] M. Posselt and J. Biersack, "Computer simulation of ion implantation into crystalline targets," *Nuclear Instruments and Methods in Physics Research Section B: Beam Interactions with Materials and Atoms*, vol. 64, pp. 706–710, Feb. 1992.

[20] P. Smulders and D. Boerma, "Computer simulation of channeling in single crystals," *Nuclear Instruments and Methods in Physics Research Section B: Beam Interactions with Materials and Atoms*, vol. 29, pp. 471–489, Dec. 1987.

[21] Ulrich Wahl, *Emission channeling: charged particle–solid interaction, detection and lattice location methods.* PhD thesis, Instituto Tecnológico e Nuclear, Nov. 2006.

[22] J. F. Ziegler, J. Biersack, and U. Littmark, *The Stopping and Range of Ions in Solids.* Pergamon Press, Jan. 1985.

[23] S. T. Picraux, L. R. Dawson, G. C. Osbourn, R. M. Biefeld, and W. K. Chu, "Strain measurements by channeling angular scans," *Applied Physics Letters*, vol. 43, p. 1020, Dec. 1983.

[24] S. T. Picraux, L. R. Dawson, G. C. Osbourn, and W. K. Chu, "Ion channeling studies of InGaAs/GaAs strained-layer superlattices," *Applied Physics Letters*, vol. 43, p. 930, Nov. 1983.

[25] C. Wu, S. Yin, J. Zhang, G. Xiao, J. Liu, and P. Zhu, "Anomalous ion channeling in InGaAs/GaAs strained heterojunction," *Journal of Applied Physics*, vol. 68, p. 2100, Sept. 1990.

[26] K. Lorenz, N. Franco, E. Alves, I. M. Watson, R. W. Martin, and K. P. O'Donnell, "Anomalous ion channeling in AlInN/GaN bilayers: Determination of the strain state," *Physical Review Letters*, vol. 97, p. 085501, Aug. 2006.

[27] X. Llopart Cudié, *Design and characterization of 64K pixels chips working in single photon processing mode [Elektronisk resurs]*. Sundsvall: Mid Sweden Unv, 2007.

[28] V. Kraus, M. Holik, J. Jakubek, M. Kroupa, P. Soukup, and Z. Vykydal, "FITPix — fast interface for timepix pixel detectors," *Journal of Instrumentation*, vol. 6, p. C01079, Jan. 2011.

[29] D. Turecek, T. Holy, J. Jakubek, S. Pospisil, and Z. Vykydal, "Pixelman: a multi-platform data acquisition and processing software package for medipix2, timepix and medipix3 detectors," *Journal of Instrumentation*, vol. 6, p. C01046, Jan. 2011.

[30] Norberto José Sobral Catarino, "Detector sensível a posição," tech. rep., Instituto Tecnológico e Nuclear, 2009.

[31] U. Wahl, "Emission channeling studies of li in semiconductors," *Physics Reports*, vol. 280, pp. 145–285, Feb. 1997.

[32] Norberto José Sobral Catarino, "Manual de operação van de graaf RBS/C (câmara pequena)," tech. rep., Instituto Tecnológico e Nuclear.

[33] J. Jakubek, "Precise energy calibration of pixel detector working in time-over-threshold mode," *Nuclear Instruments and Methods in Physics Research Section A: Accelerators, Spectrometers, Detectors and Associated Equipment*, vol. 633, Supplement 1, pp. S262–S266, May 2011.

[34] M. Mayer, "SIMNRA user's guide," Tech. Rep. Report IPP 9/113,, Max-Planck-Institut für Plasmaphysik, Garching, Germany, 1997.

[35] Peter j.m. Smulders, "FLUX7 and related programs.." http://members.home.nl/p.j.m.smulders/FLUX/HTML/.

[36] *Numerical Recipes 3rd Edition: The Art of Scientific Computing*. Cambridge University Press, Sept. 2007.

[37] A. Ramos, A. Paúl, L. Rijniers, M. da Silva, and J. Soares, "Measurement of (p,p) elastic differential cross-sections for carbon, nitrogen, oxygen, aluminium and silicon in the 500–2500 keV range at 140° and 178° laboratory scattering angles," *Nuclear Instruments and Methods in Physics Research Section B: Beam Interactions with Materials and Atoms*, vol. 190, pp. 95–99, May 2002.

[38] R. B. Stephens, "Low-temperature specific heat and thermal conductivity of noncrystalline dielectric solids," *Physical Review B*, vol. 8, pp. 2896–2905, Sept. 1973.

[39] A. Dygo, P. Smulders, and D. Boerma, "Simulation analysis of ion channeling spectra: thermal vibrational amplitude in si," *Nuclear Instruments and Methods in Physics Research Section B: Beam Interactions with Materials and Atoms*, vol. 64, pp. 701–705, Feb. 1992.

[40] T. H. Peng, Y. F. Lou, S. F. Jin, W. Y. Wang, W. J. Wang, G. Wang, and X. L. Chen, "Debye temperature of 4H-SiC determined by x-ray powder diffraction," *Powder Diffraction*, vol. 24, no. 04, pp. 311–314, 2009.

[41] H. Schulz and K. Thiemann, "Structure parameters and polarity of the wurtzite type compounds Sic—2H and ZnO," *Solid State Communications*, vol. 32, pp. 783–785, Dec. 1979.

[42] M. E. Levinshtei?n, S. L. Rumyantsev, and M. Shur, *Properties of advanced semiconductor materials: GaN, AlN, InN, BN, SiC, SiGe*. New York: Wiley, 2001.

[43] J. Jakubek, A. Cejnarova, T. Holy, S. Pospisil, J. Uher, and Z. Vykydal, "Pixel detectors for imaging with heavy charged particles," *Nuclear Instruments and Methods in Physics Research Section A: Accelerators, Spectrometers, Detectors and Associated Equipment*, vol. 591, pp. 155–158, June 2008.